Department of Physics and Astronomy
University of Heidelberg, Germany

Master's thesis in Physics

Arso Ivanovic

born in Podgorica, Montenegro

22 December 2017

Experimental observation of ultrashort laser pulse effects on the autoionization dynamics of argon atoms

This Master's thesis has been carried out by
Arso Ivanovic at the Max-Planck-Institut fur Kernphysik
under the supervision of
Prof. Thomas Pfeifer

Abstract

Experimental observation of ultrashort laser pulse effects on the autoionization dynamics of argon atoms - Within this work, electron dynamics inside argon atoms are observed by probing the autoionizing states of argon atoms, so-called window resonances, with both attosecond XUV and timed-delayed few-cycle femtosecond NIR laser pulses, using attosecond transient absorption spectroscopy. The window resonances in the energy region of 25 - 29.3 eV are first excited with the XUV pulse and then dressed by the NIR laser, where the natural decay process of the states is greatly affected by the strong-field of the NIR pulse. Preliminary results of the measurement are presented in this work, with a hypothetical description of some of the effects that are present. A comparison has been made with the experimental results from a paper publishing measurements of autoionizing states with attosecond transient absorption spectroscopy for the first time, where the same resonances were probed. The comparison is only partly possible due to different experimental parameters and conditions, where more pronounced and new effects have been observed in the here performed measurement.

Zusammenfassung

Experimentelle Beobachtung ultrakurzer Laserpulseffekte auf die Autoionisierungsdynamik von Argonatomen - In dieser Arbeit wird die Elektronendynamik in Argonatomen mithilfe von attosekunden transienten Absorptionsspektroskopie untersucht. Ein spezielles Augenmerk liegt dabei auf den Autoionisierungszustnden, den sogenannte Fensterresonanzen im Energiebereich zwischen 25 - 29,3 eV der Argonatome. Die Zustnde werden zunchst mit dem XUV-Puls angeregt und wechselwirken dann mit dem NIR-Puls, wobei der natrliche Zerfallsprozess der Zustnde durch das starke Feld des NIR-Pulses beeinflusst wird. Vorlufige Ergebnisse der Messung werden in dieser Arbeit vorgestellt, mit einer hypothetischen Beschreibung einiger der vorhandenen Effekte. Ein Vergleich wurde mit den experimentellen Ergebnissen einer anderen Verffentlichung gemacht, die Messungen von denselben Autoionisierungszustnden mit attosekunden transienten Absorptionsspektroskopie zum ersten Mal beschreibt. Der Vergleich ist nur bedingt mglich aufgrund unterschiedlicher experimentellen Parameter und Bedingungen, wobei bei der hier durchgefhrten Messung strkere und neue Effekte beobachtet wurden.

Contents

Chapter 1

Introduction

When I first started learning about the microworld of atoms and molecules I was driven right from the start to find out more about it, as I started to realize how differently it is perceived and physically described from the more familiar and tangible macroworld. Learning about the laws of quantum physics, that govern the world of microscopic particles, I started diving in deeper into that world and tried to understand the concepts and working principles of quantum mechanics. Understanding the connection between quantum and classical physics by observing different physical processes, has taught me that there is more than one way to describe some physical concepts depending on conditions of the physical system.

I have been fascinated by light phenomena early on as well, and the more I learned the more I realized the influence and effects of electromagnetic waves, especially lasers on the behavior of the particles they are interacting with. The light-matter interaction has an abundance of different types of interactions, which produce a multitude of phenomena which have a certain uniqueness, and many of them are yet to be physically described, while new ones are emerging as the science makes progress.

My work is dedicated to unraveling the mechanism of interaction between light and atoms, specifically between a strong electromagnetic field and electrons bound inside atoms. Electron dynamics inside atoms is happening on a timescale of femtoseconds or even attoseconds ,where 1 fs=$10^{-15}s$ and 1 as=$10^{-18}s$. These belong to the fastest processes that exist in nature. The atomic unit of time is about 24 as. Therefore atomic units are commonly used in this regime. In order to capture such processes a probe just as fast is necessary. The probe has been found to be the ultrashort laser pulse, which only lasts for a few femtoseconds or even has pulse duration of attoseconds. There is a specific method for producing such ultrashort pulses, described later in the thesis.

Different techniques exploit these ultrashort pulses in order to study how they interact with a physical system. In our laboratory, they are interacting with an ensemble of atoms or molecules in a gaseous state. We are using only one target species at a time, since every chemical element has a particular behavior that is unique to it and that needs to be investigated. I will describe our technique in chapter 2. It is absorption spectroscopy that we use in order to observe the effects

of interactions, where we have typical pump-probe mechanism, where there are two different laser pulses, one being a pump that excites the system to some states and the other being a time delayed probe that modifies the dynamics of de-excitation of the system. There is the ability not only to capture but also to control processes with these lasers, which can alter the properties of atoms and molecules. A ubiquitous example is altering of the natural lifetime of some excited states of atoms and molecules. It has been shown that interactions of electrons are highly dependent on the laser intensity, and therefore a strong field is usually necessary in order to impose significant changes to the investigated system. Many new insights have been brought to light in recent years by studying different processes. Along the way, many techniques for laser pulse characterization have been developed in order to accurately describe laser pulse and its interaction with the system.

In the second chapter theoretical background will be given, which is chosen to be of most importance for the following chapters of the thesis. The third chapter describes our experimental setup in detail, where there is a section on the characterizing the newly designed Kapton filter as part of my project. In this chapter attosecond transient absorption is also introduced. The fourth chapter is focused on the in-situ intensity calibration of our driving NIR laser, which is of importance for future measurements. This also applies to the measurement performed in this work, which constitutes chapter five as the main part of the thesis. The measurements were performed in argon as target gas, where the autoionizing states of the noble gas argon, so-called window resonances, are probed with the above mentioned technique.

Chapter 2

Theoretical background

The most common approximation for the shape of the temporal envelope of a coherent laser pulse and its transverse spatial profile is that they are Gaussian functions. For a Gaussian pulse the relation between peak power P_0 and pulse energy ϵ is given by $P_0 = 0.94 \cdot \frac{\epsilon}{\tau}$, where τ is the pulse duration. Pulse duration is normally defined as the FWHM (full width at half maximum) of the optical power versus time.
The optical intensity is the optical power per unit area transmitted through an imagined surface perpendicular to the propagation direction. Optical intensity and power are normally taken as quantities averaged over one oscillation cycle. The shape of the intensity profile of a laser beam is usually measured by a beam profiler.

A Gaussian transverse intensity profile of cylindrically symmetric laser beam is given by

$$I(r) = I_0 e^{-2(\frac{r}{W})^2} \tag{2.1}$$

where the radius W at $I = \frac{I_0}{e^2}$ is a measure of the beam size, I_0 is the peak intensity. The intensity of a pulsed laser beam is a function of both space and time. For a Gaussian pulse, the intensity can be expressed as

$$I(r,t) = \frac{1.88\epsilon}{\pi W^2 \tau} e^{-2(r/W)^2} e^{-4ln2(t/\tau)^2} \tag{2.2}$$

The peak intensity at the center of the beam is

$$I_{0p} = \frac{1.88\epsilon}{\pi W^2 \tau} \tag{2.3}$$

The formulas in this section are taken from [1].The smallest spot size a linearly polarized laser beam can be focused to theoretically is half the laser wavelength due to the diffraction from the limited aperture of the focusing optics. It was thought that the shortest pulse that can be generated is one optical cycle, until sub-cycle pulses were produced [2].

The electric field of a coherent optical pulse is given by:

$$\varepsilon(t) = E(t) cos[\omega_0 t + \phi(t)] \tag{2.4}$$

where $E(t)$ is the amplitude (envelope), ω_0 is the carrier (central) angular frequency, and $\phi(t)$ is the temporal phase. A pulse is said to be Fourier transform limited when

the temporal phase equals a constant or is a linear function of time.
A pulse is said to be chirped when its instantaneous frequency changes with time. The instantaneous frequency is defined as:

$$\omega(t) \equiv \frac{d}{dt}[\omega_0 t + \phi(t)] \tag{2.5}$$

The pulse can be positively or negatively chirped depending on the chirp parameter, which means that the instantaneous frequency increases or decreases with time, respectively. This is depicted in figure 2.1.

In the frequency domain the electric field is obtained by performing a Fourier

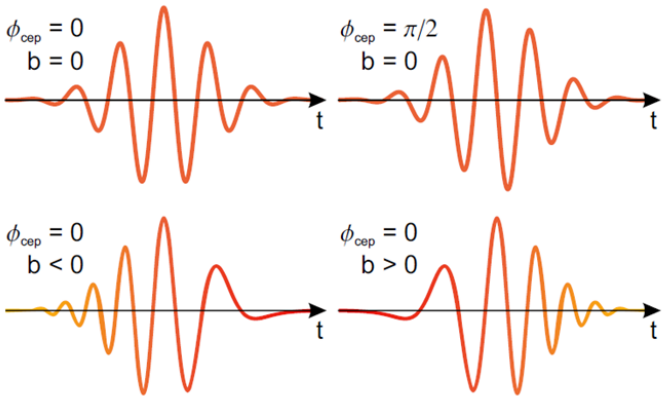

Figure 2.1: Top two pulses are unchirped with two different CE phases (defined below), and the bottom two are positively and negatively chirped pulses, where b is the chirp parameter

transform of the field in the time domain

$$\tilde{E}(\omega) = \int \varepsilon(t) e^{-i\omega t} dt. \tag{2.6}$$

and in general

$$\tilde{E}(\omega) = U(\omega) e^{i\varphi(\omega)}, \tag{2.7}$$

where $U(\omega)$ is the spectral amplitude, and $\varphi(\omega)$ is the spectral phase. The inverse Fourier transform brings the field back to the time domain

$$\varepsilon(t) = \int \tilde{E}(\omega) e^{i\omega t} d\omega. \tag{2.8}$$

2.1 Ultrashort pulse dispersion

The well known Heisenberg time-energy uncertainty priniciple

$$\Delta t \Delta E \geq \hbar \tag{2.9}$$

which shows that the smaller the uncertainty in time the greater the uncertainty in energy, and vice versa, manifests itself in the case of laser pulses. Here we have

pulse duration and spectral bandwidth as observables in the uncertainty relation. The time-bandwidth product of a pulse is the product of its temporal duration and spectral width (in frequency space). Defined rather qualitatively as opposed to the previous section, a bandwidth-limited optical pulse (or transform-limited pulse) is a pulse which has the minimum possible pulse duration for a given spectral bandwidth, or has a minimum possible spectral bandwidth for a given pulse duration. Such a pulse has the smallest time-bandwidth product. This limitation is a consequence of the uncertainty relation with the equality sign setting the lower limit. If an initially transform-limited pulse propagates through a medium, its time-bandwidth product can increase due to the influences of chromatic dispersion or nonlinearities.

Chromatic dispersion of an optical medium is a phenomenon that the phase velocity and group velocity of light propagating in a transparent medium depend on the optical frequency. It results mostly from the interaction of light with electrons of the medium, but can also appear due to geometrical effects. The attribute "chromatic" is used to distinguish it from other types of dispersion relevant for optical fibers.
A frequency-dependent refractive index means that the phase velocities of each frequency component of an ultrashort pulse are different. When a transform-limited pulse propagates through a dispersive medium a quantity called spectral phase is defined by

$$\varphi(\omega) = -\beta(\omega)L \tag{2.10}$$

where L is the propagation length in the medium and the propagation constant, which is the phase shift per unit length is

$$\beta(\omega) = \frac{\omega}{c} n_I(\omega) \tag{2.11}$$

It can be expanded in a Taylor series

$$\beta(\omega) = \beta(\omega_0) + \frac{d\beta}{d\omega}|_{\omega_0}(\omega - \omega_0) + \frac{1}{2}\frac{d^2\beta}{d\omega^2}|_{\omega_0}(\omega - \omega_0) + ... \tag{2.12}$$

The first term is a constant phase shift which determines the phase delay of the carrier wave. The phase velocity is $\nu_p = \frac{n_I(\omega)}{c} = \frac{\beta(\omega_0)}{\omega_0}$. The derivatives of the spectral phase, the so-called phase derivatives, are denoted by

$$\begin{aligned} GD &= \frac{d\varphi(\omega, L)}{d\omega}|_{L,\omega_0} \\ GDD &= \frac{d^2\varphi(\omega, L)}{d\omega^2}|_{L,\omega_0} \\ TOD &= \frac{d^3\varphi(\omega, L)}{d\omega^3}|_{L,\omega_0} \end{aligned} \tag{2.13}$$

They are group delay(GD), group-delay dispersion (GDD), and third order dispersion (TOD). Figure 2.2 shows the effects of them on the carrier wave and envelope. The shape of the pulse in the case of TOD is calculated numerically. Group velocity dispersion (GVD) is defined as $GVD = GDD/L$. As you can see in the figure,

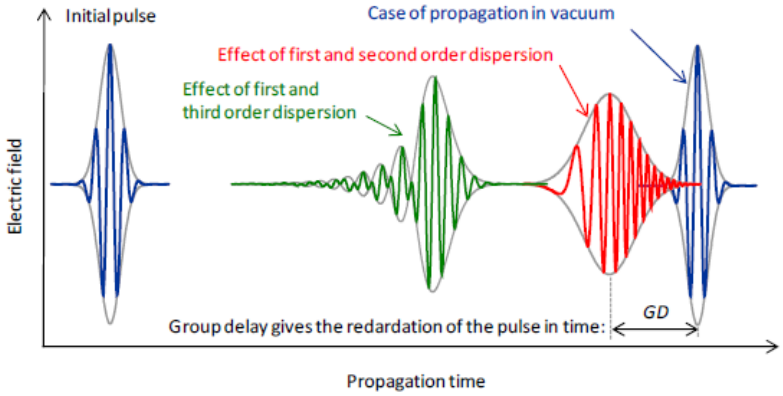

Figure 2.2: Schematic showing the temporal effect of the first three phase derivatives on the pulse structure. Taken from [3]

GVD or GDD is responsible for the pulse chirp, and TOD and higher-order terms are responsible for creating additional structures as pre-pulses and post-pulses.
The carrier-envelope phase (CEP) is defined as the phase of the electric field at the peak of the pulse envelope. It can be approximated by

$$CEP = \varphi(\omega_0, L) - GD \cdot \omega_0 \tag{2.14}$$

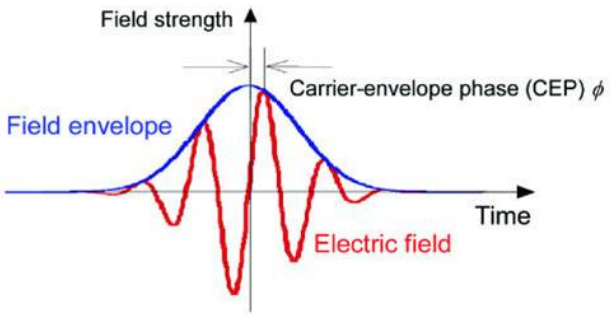

Figure 2.3: definition of carrier-envelope phase of a few-cycle optical pulse. Taken from [4]

2.2 Ionization of atoms in intense laser fields

This section describes different types of ionization of atoms due to interaction with a high-intensity laser pulse, where the regime of intensities of interest is $10^{12} - 10^{15}$ W/cm^2. In the following many interesting phenomena that emerge in this strong field regime are described.

2.2.1 Ponderomotive potential

If we have a free electron exposed to an oscillating electric field, nonrelativistically its motion is described by

$$m_e \frac{dv}{dt} = eE_0 cos\omega_L t \tag{2.15}$$

where m_e is the electron mass, ω_L the laser frequency, E_0 is the electric field amplitude and v and e are the electron velocity and charge. The cycle averaged kinetic energy of the electron U_p inherent to this motion is called the ponderomotive potential, and it can easily be calculated by

$$U_p =< \frac{1}{2} m_e v^2 >= \frac{e^2 E_0^2}{4 m_e \omega_L^2} = \frac{e^2 I}{2\varepsilon_0 c m_e \omega_L^2} \tag{2.16}$$

The ponderomotive potential is a function of the laser intensity and frequency. U_p raises the ionization potential of an atom or molecule, so there is an effective potential $I_{eff} = I_p + U_p$ that needs to be overcome.

2.2.2 The Keldysh parameter

Nonlinear ionization of atoms by intense electromagnetic fields is described by Keldysh theory, whose original work is found in [5]. It is usually applied to low-frequency fields, which means that the ionization potential I_p is much larger than the photon energy $\hbar\omega$, i.e. the multiquantum parameter is large:

$$K_0 = I_p/\hbar\omega \gg 1. \tag{2.17}$$

An independent dimensionless parameter was introduced by Keldysh and is known as the Keldysh parameter:

$$\gamma = \frac{\omega_L \sqrt{2 m_e I_p}}{e E_0} = \sqrt{\frac{I_p}{2 U_p}} \tag{2.18}$$

with the electric field $E(t) = E_0 cos\omega_L t$. It represents a ratio of the characteristic atomic momentum $\hbar\kappa = \sqrt{2 m_e I_p}$ to the field induced momentum $p_F = eE_0/\omega_L$. Defined in another way, it is the ratio of the time the electron travels the distance $b_0 = I_p/eE_0$ moving with the atomic velocity $v_{at} = \sqrt{2I_p/m_e}$. The value b_0 is the width of a static barrier created by the field E_0, so $\tau = b_0/v_{at} = \gamma/\omega_L$ is the time of flight under the barrier or the Keldysh tunneling time, which will be discussed further down.

2.2.3 Multi-photon and above threshold ionization

An atom can be photoionized by absorbing a single photon whose energy is higher than or equal to the ionization energy of the atom. A different process, multi-photon ionization (MPI), results from the simultaneous absorption of several photons and it was introduced in physics due to the theoretical prediction of two-photon transitions

and the discovery of the laser. It happens in a strong laser field when the photon energy is lower than the ionization potential of the atom, so that single-photon ionization is absent, and the Keldysh parameter in this regime is $\gamma \gg 1$. This process is schematically shown in figure 2.4. This highly nonlinear process is described with

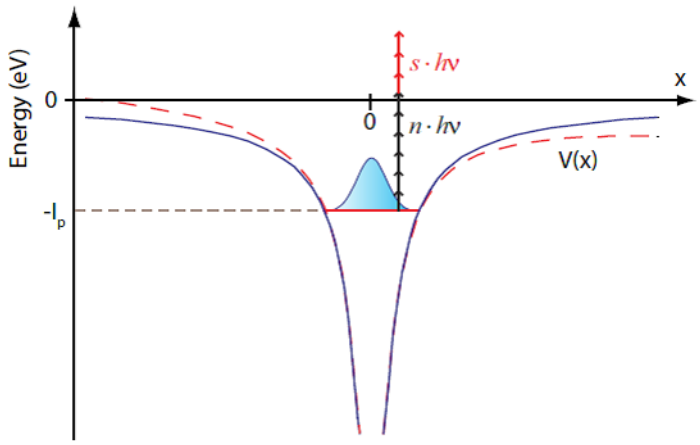

Figure 2.4: Multi-photon ionization by absorption of N photons of energy $h\nu$ and above threshold ionization by absorbing N+S photons. V(x) is the atomic potential shown without the laser field (blue line) and with the laser field (dashed red line). Taken from[6]

an N-photon ionization rate:

$$\Gamma_N = \sigma_N \cdot I^N \tag{2.19}$$

where σ_N is the N-photon ionization cross-section and I the laser intensity. For higher intensities the non-perturbative regime of MPI is called above threshold ionization (ATI). ATI is the case where the bound electron absorbs more photons than the minimum number required to reach the ionization threshold. Excess photons (red arrows) are absorbed , which was unexplained since a free electron cannot absorb photons because of the law of momentum conservation. But it has been shown that the electron absorbs photons while it is still in the Coulomb field of the parent ion which provides momentum transfer. The photoelectron energy spectrum consists of equidistant peaks separated by the photon energy. The ATI-rate originating from the absorption of N + S photons is proportional to:

$$\Gamma_{N+S} \propto I^{N+S} \tag{2.20}$$

2.2.4 Tunnel and barrier suppression ionization

The limit $\gamma \ll 1$ is known as the tunneling domain. The Coulomb potential V(x) is tilted by a strong enough electric field of the laser, where a potential barrier is formed through which the electron can tunnel, as shown in Figure 2.5. The $\gamma \ll 1$ limit denotes that the oscillation period of the laser field is much longer than the Keldysh tunneling time of the electron. The tunneling limit is often called the quasistatic or

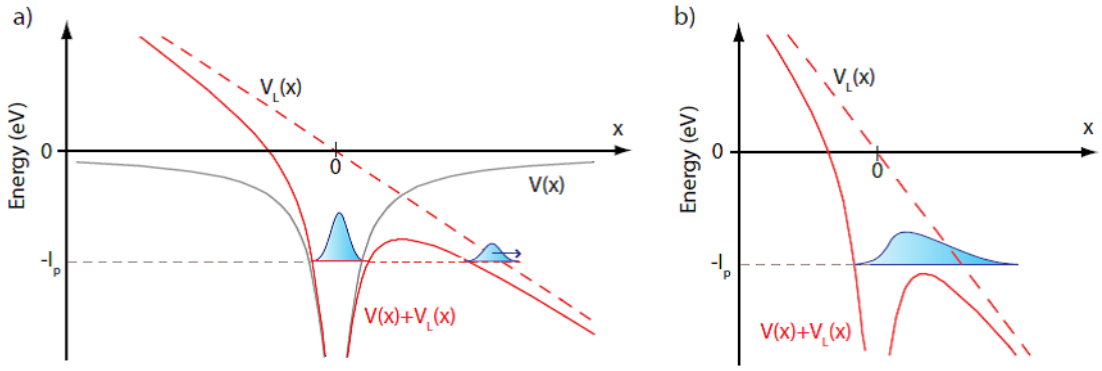

Figure 2.5: Schematic diagram of strong-field photoionization for $\gamma \ll 1$ illustrating a) tunnel ionization and b) barrier suppression ionization.Taken from [6].

adiabatic regime of ionization, where time can be treated as a parameter. The most commonly used method to describe the tunnel ionization is ADK-Theory where it can be shown that significant ionization happens during a single half laser cycle and predominantly around the electric field peak corresponding to the lowest barrier.

Barrier suppression ionization (BSI) (or over-the-barrier ionization) occurs when the laser electric field is higher than the characteristic electric field of the atomic system and hence the ground state is no longer bound. The initial wavepacket escapes classically over-the-barrier as sketched in Figure 2.5. The critical intensity necessary to achieve barrier suppression ionization can be expressed as:

$$I_{BSI}[W/cm^2] = 4 \cdot 10^9 (I_p[eV])^4 Z^2 \tag{2.21}$$

where Z denotes the charge state of the atom or ion (for ionization of neutral atoms Z equals one). The formula is taken from [6]. This shows that even with the most intense lasers it is not possible to fully strip heavy elements.

2.3 High harmonic generation

When a linearly polarized short laser pulse with a high enough intensity interacts with noble gases, odd harmonics of the fundamental frequency emerge as a sequence of attosecond pulses in the time domain. Noble gases are used because of their large binding energies. The harmonic spectrum is depicted in figure 2.6.
In the three-step model description of high-order harmonic generation (HHG) an electron is first liberated from an atom through tunnel ionization, accelerated by the laser field, and subsequently recombines with the parent ion, emitting any excess energy as a high-energy photon, which is depicted in figure 2.7 a) and b). Described in detail, first the electron tunnels through the barrier around each oscillation peak of the laser electric field when the potential barrier is the lowest and thus the ionization rate the highest. A laser pulse of many optical cycles creates wavepackets at different instants which thus all have different trajectories, but few-cycle pulses create wavepackets only around the peak of the field where the ionization is significant.

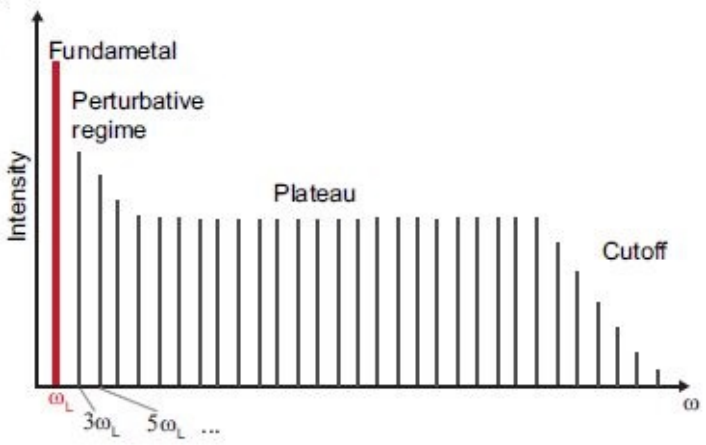

Figure 2.6: Schematic of high-harmonic spectrum with the perturbative regime, plateau region and the cut-off region with the highest photon energy. Taken from [6].

The free wavepacket is propagating away from the ion until after a quarter of the laser period it is pulled back by the laser field because the electric field had reversed its direction. The highest-energy portion of the wave packet re-collides with the bound-state portion of the same wavepacket near the second zero crossing of the laser field (counting from the wavepacket's birth) as shown in figure 2.7 c) by gray arrows, and results in the emission of highest energy (cut-off) soft X-ray photons. Worth to mention is also that the returning wavepacket is heavily chirped and its duration is about 1 fs, which is longer than the duration of the originally released wavepacket.

This semiclassical three-step model is based on the single active electron (SAE) approximation, where it is assumed that only one electron participates in the ionization of the atom or molecule by a low frequency field. Other electrons screen the nucleus introducing an effective single-electron potential. This approximation is most applicable for noble gases, where multielectron exicitation energies are large compared to the laser frequency and single excitation energies.

To better understand the quantum nature of the process it is argued that the continuum part of the returning electron wavefunction can interfere with the bound part of the same wavefunction. This interference results in fast oscillations of the electron density as illustrated in fig. 2.8. The dipole moment of the atom induced in this way contains these fast oscillations in one of its terms, which is described more in [7]. Since the maximum energy of the returning electron is $W_{max} = 3.17U_p$, the maximum emitted photon (cut-off) energy is given by:

$$E_{cut-off} = I_p + 3.17U_p \tag{2.22}$$

where I_p is the ionization potential of the atom and U_p is the ponderomotive energy of the electron in the laser field. For NIR and IR lasers, W_{max} can reach hundreds and thousands of eV, respectively. Quantum mechanically, photons are emitted with

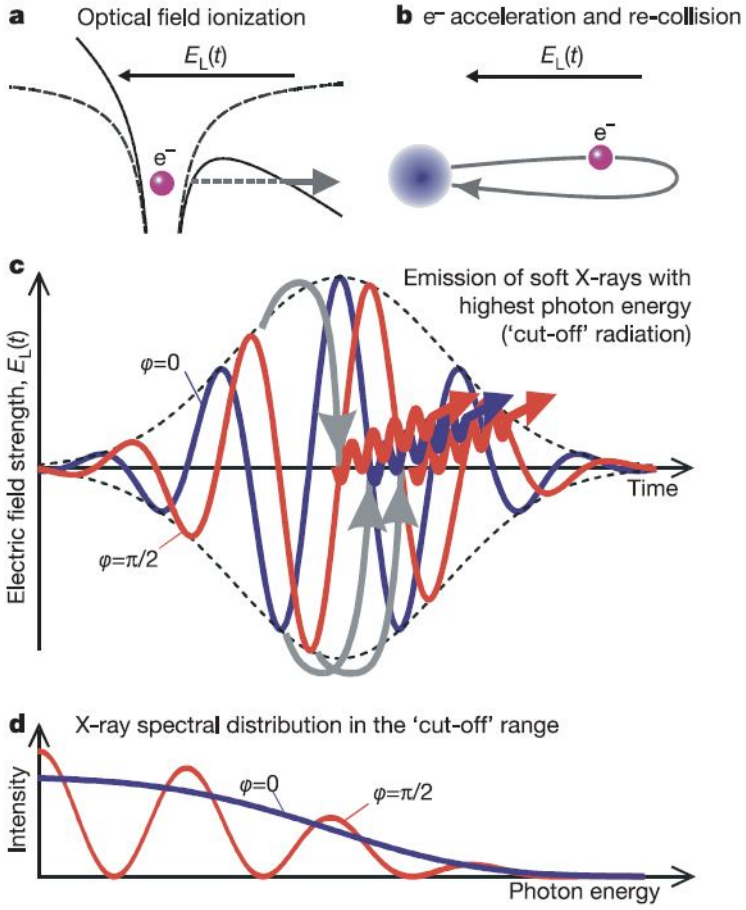

Figure 2.7: a) Schematic of the first step of the three step model, where a Coulomb potential is suppressed around the crest of the strong field, and the electron can tunnel through the potential barrier or be set free by BSI. Atoms exposed to a few-cycle pulse emit one or several wave packets near the pulse peak, depending on the peak intensity (relative to the ionization threshold) and the C-E phase φ. b)The freed electron is moved away from the atomic core and after a quarter cycle pulled back by the field that had reversed its sign. It can then recollide with the parent ion and one of the processes that follow is the emission of a soft X-ray photon. c) The highest-energy (cut-off) X-ray photons are emitted near the second zero crossing of the laser electric field (counting from the wavepacket's birth). With $\varphi = 0$ (cosine waveform, blue line) they are temporally confined to one single burst, whereas $\varphi = \pi/2$ (sine waveform, red line) yields two bursts of comparable amplitude. d) The spectral distribution of the emitted 'cut-off' X-rays is continuous or modulated quasi-periodically, respectively. Taken from [8]

energies even above the classical cut-off energy, where the intensities are exponentially decreasing as the photon energy grows. In this range the temporal chirp is practically negligible, which means that by filtering the highest energy photons by a bandpass filter isolated attosecond bursts are produced for a cosine-shaped few-cycle

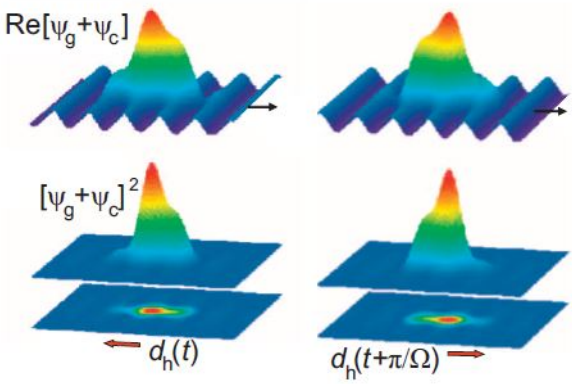

Figure 2.8: The recolliding continuum part of the electron wave function ψ_c interferes with its ground state part ψ_g, and this is shown at two instants, t and $t + \pi/\Omega$. Top and bottom images are the real part of the total wavefunction and the electron density, respectively. Interference causes density oscillations which induce a dipole moment of the atom. Taken from [7].

driving pulse.

2.3.1 Phase-matching

For phase-matched HHG in an ensemble of atoms the phase velocities of the fundamental driving laser, and the harmonic light, must ideally be matched. Phase-matched signal ensures that harmonic emission from many atoms over an extended medium adds together coherently. This is achieved only with a stabilized CE phase, with minimal phase variation for a fraction of the laser cycle within which the electron can return. In HHG the nonlinear medium is ionized as harmonics are emitted, which results in a varying index of refraction and therefore dispersion. Without phase-matching, the evolution of the electric field due to geometrical and nonlinear dispersion leads to a variation in the moment of birth and re-collision of the electron. There is a geometrical Gouy phase that results in a dynamical change of CEP. Therefore the geometry of the interaction medium setup is important, where we have an HHG cell which minimizes the curvature of the laser and HHG wavefront, which leads to a phase-matched output.

2.4 Autoionization

Fano's theory of configuration interaction [9] describes a bound state $|\varphi\rangle$ which is embedded within a set of continuum states, and it is modified by this interaction. In this work, this so-called autoionizing state is a bound state involving excitation of one inner-shell electron or two electrons whose total excitation energy is above at

least the first ionization threshold. The state becomes unstable against ionization with one electron being extracted. From Fano's time-independent theory one can get a quantity called reduced energy variable of the autoionizing state:

$$\varepsilon = \frac{E - E_0}{\Gamma/2} \tag{2.23}$$

where E_0 and Γ are the position and width of the resonance, respectively. Another quantity called the asymmetry parameter q describes the asymmetric Fano line shape (see figure 2.9), which results from the interference between the direct transition to the continuum and the transition to the autoionizing state.

$$q = \frac{\langle \Phi | D | g \rangle}{\pi \cdot V_E^* \langle c | D | g \rangle} \tag{2.24}$$

where $|g\rangle$ is the ground state, $|c\rangle$ is a set of continuum states, $|\Phi\rangle$ is the modified bound state, D and V_E^* represent the electromagnetic and configuration interaction, respectively. The q parameter is a measure of importance of the direct transition from the initial state to the continuum states compared to the transition via the autoionizing state. High q means weak direct transition and hence symmetric line shape since the interference is minimized. The relative transition probability is given by

$$\frac{|\langle \Psi | D | g \rangle|^2}{|\langle c | D | g \rangle|^2} = \frac{|q + \varepsilon|^2}{1 + \varepsilon^2} \tag{2.25}$$

In the literature, the minimum of the line is usually referred to as a window, because of the appearance of such resonances in photographic spectra, and the term is a useful one because it avoids confusion with other types of minima in the absorption cross section.
In the extreme case q=0, which means that the transition via the autoionizing state is suppressed, while finite configuration interaction still occurs, the destructive interference causes the relative transition probability to always be smaller than unity. The corresponding state is called a window resonance. Far from resonance the relative transition probability is approaching unity, therefore the bound state can only impact the surrounding continuum states within the autoionization width.

The minimum of an autoionizing line is at zero in the cross section in the simple case of a resonance interacting with a single continuum. This is preserved when a Rydberg series of autoionizing resonances interacts with a single continuum but the minimum is shifted when more continua are present. For this reason, it is desirable to study autoionizing resonances and the interactions between them just above the first ionization threshold, where the number of open continua channels is minimal. The absorption cross section of an autoionizing resonance is given by a Beutler-Fano profile

$$\sigma = \sigma_a \frac{|q + \varepsilon|^2}{1 + \varepsilon^2} + \sigma_b \tag{2.26}$$

where σ_a and σ_b represent two parts of the cross section that correspond to the transitions of the continuum that do and do not interact with the discrete autoionizing

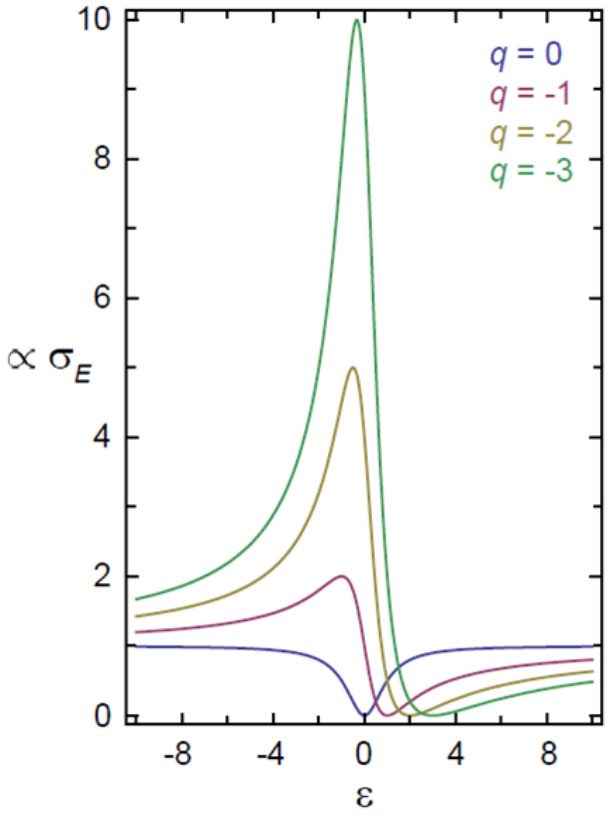

Figure 2.9: The Fano line shape cross section (eq.2.26) shown for different q parameters as a function of the reduced energy ε, where for q=0 it is an inverted Lorentzian line shape representing a window resonance. Taken from [16]

state, respectively. A correlation coefficient ρ^2 gives the portion of the continuum which interacts with the autoionizing state

$$\rho^2 = \frac{\sigma_a}{\sigma_a + \sigma_b} \tag{2.27}$$

2.5 Autoionization in a strong field

When an autoionizing resonance is exposed to a strong field, non-perturbative effects such as Rabi cycling are expected to occur. An effective Rabi frequency is defined, which directly incorporates autoionization because the modified bound state is used. More is found in [10]. Interference effects due to mixing with continuum are encoded into the Rabi frequency. This makes a difference between the strong-field driven dynamics of an autoionizing from that of a bound state.
The case of strong coupling of two autoionizing states is shown in figure 2.10 . In general, $|a\rangle$ and $|b\rangle$ are assumed to be coupled to different continua. A second radiation field couples the two states. Other transitions from the bound states to different continua are also happening as shown by arrows. Coupling to different

continua can be neglected for moderate intensities.

In our case we have an approximation in which one of the fields is weak while the

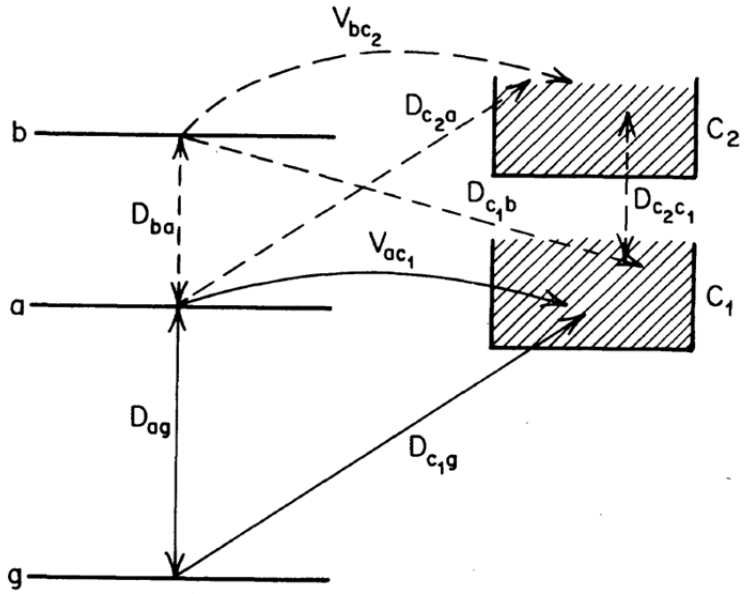

Figure 2.10: Schematic of two autoionizing states coupled to electromagnetic fields. D and V denote electromagnetic and configuration interactions, respectively. The shaded areas are the continua to which the states are coupled. Taken from [10]

other is strong. This situation means that very few atoms are excited per unit time from the ground state $|g\rangle$ to $|a\rangle$, and further processes are determined by the strong field. In a weak field the transition probablility per unit time is time-independent. If we have a long enough interaction time and we have a certain q value we can see that the line shape of an autoionizing resonance is a function of intensity, where one effect is a shift of the minimum of the line with intensity increase. The intensity modifies the interference between channels by affecting some transitions but not the configuration interaction. The shifting of minimum is viewed as a separate effect from ac Stark shifting. For weak fields, transition probability per unit time is linear in the light intensity. When the field becomes strong, the process is not proportional to the intensity anymore, the resonant states experience ac Stark shifts which can become larger than Γ.

In the case of two autoionizing resonances which are excited by a weak field and resonantly coupled by a strong field the interference between direct ionization of $|a\rangle$ and ionization via $|b\rangle$ and its configuration interaction causes two peaks of one resonance, appearing due to ac Stark splitting, to have unequal widths. As the intensity increases one of the peaks continues to narrow while the other continues to broaden. So of the two dressed states created by strong coupling one acquires a short and the other a long lifetime against ionization. More is given in [10].

2.6 Stark shift and laser-induced line shape change

The Stark effect is the shifting and splitting of spectral lines due to the presence of an external electric field. Stark effect in a variable field differs greatly from the analogous effect in a static electric field. In a static field the perturbation of a non-degenerate bound atomic state reduces to an energy shift of that state. In a monochromatic EM field the initial non-degenerate state is turned into a set of energy states with the distance between adjacent levels equal to the photon energy. The entire energy spectrum is shifted with respect to the unperturbed level. Another distinction is that resonance can happen when the EM field frequency is close to the transition frequency to another bound state. Even in a weak field the resonant level may be significantly populated (saturation effect) and this is accompanied by the splitting of both the initial and resonant level into two energy levels (Rabi effect).

An ac Stark shift normally refers to a cycle averaged energy shift of a state induced by a monochromatic electric field. For a few-cycle laser pulse the cycle averaged energy shift loses meaning since the intensity changes quickly from one cycle to another, and the energy levels will instead undergo a time-dependent energy shift. For a short pulse, the distribution width of the energy shift is inversely proportional to the pulse duration. Therefore, the estimated Stark shift should only reflect the energy shift averaged over the entire envelope of the NIR pulse.

Given the above we can argue that a short pulse cannot precisely control the energy of a quantum system. Still, it can impose a phase onto a particular state at a defined moment of time, which enables control of absorption dynamics in light-matter interaction.

If we now consider our XUV-NIR pump-probe configuration, which will be explained in the next chapter, it can be assumed that to lowest order, one can ignore the laser-induced change of the population of the XUV-excited bright (dipole-allowed) state and only include a laser-induced modification of the bright state phase. The light-induced phase (LIP) is dependent on both time and delay. The Stark shift $\Delta E(t, \tau)$ of the bright state that results from the laser-coupling to nearby states is the origin of this phase:

$$\phi(t, \tau) = \int \Delta E(t, \tau) dt. \tag{2.28}$$

More is found in [11].The light-induced phase gives rise to a phase shift of the time-dependent dipole moment regarding to the XUV-only case. In the time domain, this phase shift means that the response electric field that is generated in the absorbing medium is no longer exactly out of phase with the driving XUV field. This means that the absorption line shape will no longer be a positive and symmetric curve centered on the resonance frequency, but it can generally have both positive and negative values.

One should consider the simplest LIP, a constant phase ϕ, as proposed by Ott [12]. Christian Ott and others proposed that it might be possible to see a line shape change from completely Lorentzian to completely dispersive and back again. This has been shown both theoretically and experimentally for some autoionizing states of helium [14].

There a several few-level models to calculate the Stark shift. In [12] the ponderomotive shift, which has been used later in the thesis, was proposed as the simplest model. It works for non-resonant coupling of loosely bound states. The rotating wave approximation (RWA) is more appropriate when the coupling laser is close to resonance with the bright-dark state transition, which includes Rabi cycling of the population between two coupled states, whereas second order perturbation theory (SOPT) is more suitable in the far off-resonance situation.

Chapter 3

Experimental setup and ATAS technique

3.1 Femtosecond laser system

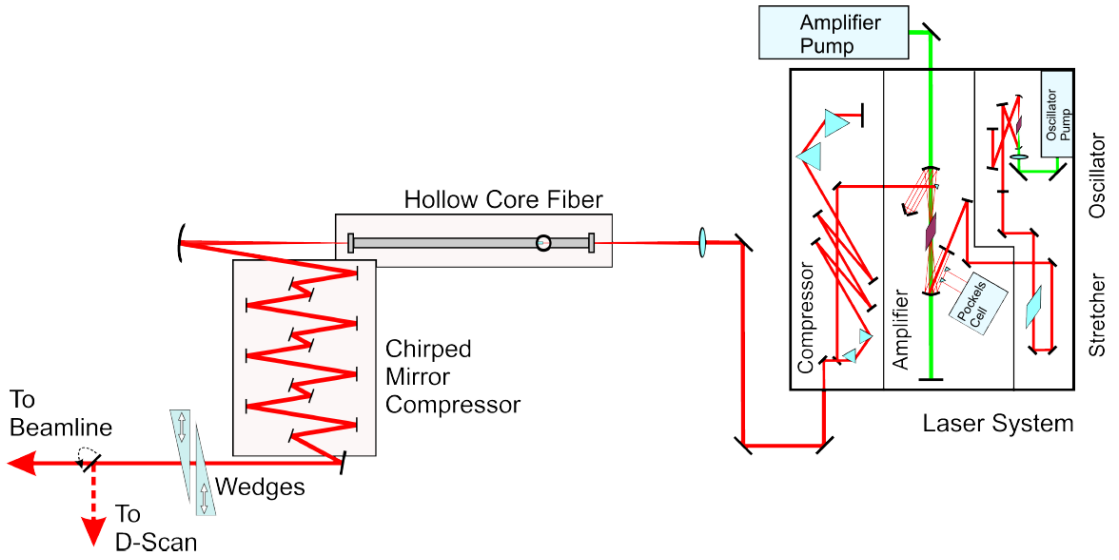

Figure 3.1: A schematic of our ultrashort laser production process. Seed pulses are produced in the oscillator, pass the stretcher and enter the multipass amplifier, where a Pockels cell picks out every 20000th pulse to be amplified further in a 10th pass through the amplifier crystal. Subsequently a grating compressor with four additional TOD mirrors shorten pulses. Spectral broadening happens in the hollow-core fiber filled with helium, and recompression is done with chirped mirrors and fine tuned with wedges. Taken from [15]

Our laser system is called Femtopower^{TM} HR/HE CEP, manufatured by Femtolasers GmbH. It produces CEP stabilized, sub-20 fs pulses with pulse energy 3 mJ with 3 kHz repetition rate.

A sketch of the setup is shown in the figure. An oscillator system delivers already CEP-stabilized lasers pulses shorter than 10 fs at 75 MHz repetition rates, with pulse energies around 1 nJ. The pulses are amplified by chirped pulse amplification (CPA) in the multipass configuration. The pulses from the oscillator are stretched in time up to several picoseconds and are then propagated 10 times through an amplifying gain medium, which is pumped using a high power Q-switched pump laser. Gain narrowing occurs, which means that only the central part of the spectrum is efficiently amplified, so the spectral bandwidth decreases. After that the pulses are compressed by a grating compressor, almost to their bandwidth limit < 20 fs. At the cost of a lower rep rate 3 kHz, the pulse energy is increased from nJ to 3mJ. The gain medium in both the oscillator and the amplifier is a titanium-doped sapphire crystal (Ti:Al2O3 or Ti:Sa), able to amplify almost octave broad light, centered around 800 nm. In order to compensate for dipersion of different optical elements and the crystal, negative dispersive elements such as TOD mirrors and chirped mirrors are part of the setup. Environmental conditions (thermal and humidity drifts, dust particles) affect the performance of the laser. A monitoring and control system was set up for tracking parameters such as pump laser power along with its focal spot profile, the spectrum of the oscillator pulses, etc.

To further shorten the pulse duration down to the few-cycle regime, the frequency spectrum of the pulse needs to be broadened. Thus, the next part of our apparatus is the hollow-core fiber whose purpose is to spectrally broaden the pulses. The laser pulses are focused onto the entrance of a glass capillary in order to propagate with high peak powers in the interaction medium over a long distance of 1 m. The fiber is filled with helium from one side with a pressure of around 3 bar and differentially pumped to the entrance side down to 10 mbar. Laser pulses of high peak intensity on the order of $10^{14} W/cm^2$ interact nonlinearly with the gaseous medium. After that the spectrum is recompressed by using chirped mirrors and finally glass wedges to fine tune the process by compensating dispersion. Due to the high density of free electrons in the ionized medium, plasma-iduced spectral blue-shift occurs which means that the spectrum is shifted to smaller wavelengths.
The following step is to characterize our pulses by performing a dispersion scan (D-scan).In the D-scan method, the second harmonic generation (SHG) spectrum of the laser is recorded as a function of the amount of glass the laser pulses pass through, controlled with a pair of wedges. An example of a retrieved laser spectrum is shown in figure 3.2. By knowing the input spectrum of the laser and the dispersion characteristic of the glass wedges (fused silica), an algorithm extracts the spectral phase of the laser pulse by fitting a calculated SHG spectrum to the measured spectrum.

3.2 Attosecond pulses production

The production of attosecond pulses by high harmonic generation is challenging process, but with time it became easier to perform with improvements in laser characteristics and technological advances. This process has to take place under

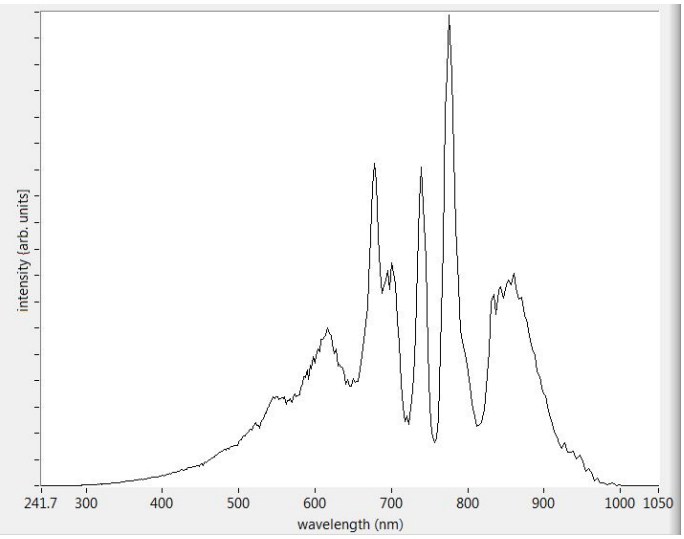

Figure 3.2: The D-scan measured wavelength spectrum of the NIR laser, with only an approximately calibrated wavelength axis.

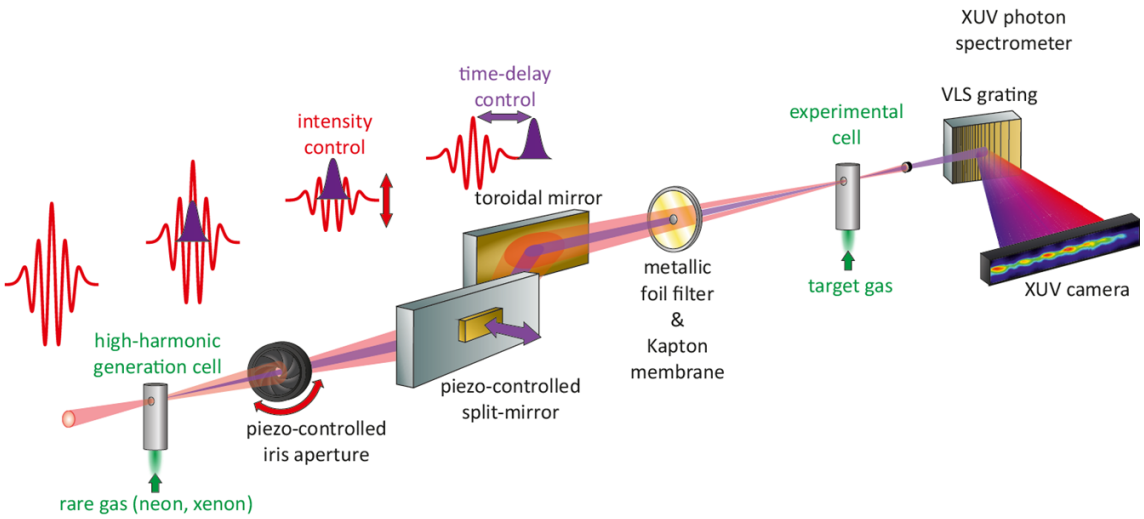

Figure 3.3: An illustration of beamline from the HHG cell to the XUV camera. Figure by Max Hartmann.

vacuum conditions, due to the fact that XUV radiation is quickly absorbed by a gaseous medium, being high energy radiation , above any ionization potential of atoms and molecules. As a rule of thumb, a vacuum pressure of 10^{-3} mbar is enough for neglecting absorption. At the HHG chamber entrance, the laser pulse energy reaches approximately 1 mJ. With the beam focused by a sliver-coated spherical mirror (f = 50 cm) down to $\sim 60\ \mu m$ focal spot size at the HHG cell, peak intensities around $10^{14} - 10^{15} W/cm^2$ are reached. The HHG cell is a 2 mm inner diameter stainless-steel tube with machine-drilled 150 m diameter holes for the laser beam to pass through. The cell is filled with a noble gas, argon for the experiments presented

in this thesis. Precision movement of the cell position along the propagation axis of the laser, referred to as the z-axis, and tuning the wedges in front of the beamline for maximum conversion efficiency, XUV light bursts emerge out of the HHG generation region. A backing pressure of about 70 mbar is applied to the cell.
A motorized iris aperture is placed in the beam path of co-propagating NIR and XUV pulses leaving the HHG chamber. Since the XUV beam has a much lower divergence, it passes through pinhole of the iris, whereas the passage of a much more divergent NIR pulse is controlled by the iris. The iris is opened in steps and after a certain iris positon the whole beam is let through. This position is known with some uncertainty. Intensity calibration has been performed in this thesis as a function of iris position.
The interferometric mirror setup consists of two grazing-incidence mirrors. One pair of flat mirrors, called the split mirror, that creates a time delay between the XUV and NIR pulses, and another toroidal-shaped mirror to refocus both beams onto the target position. The split mirror has a high reflectivity of the whole XUV spectral range due to grazing incidence. The disadvantage of grazing incidence geometry is the beam walk-off which is caused by the movement of the inner mirror. The

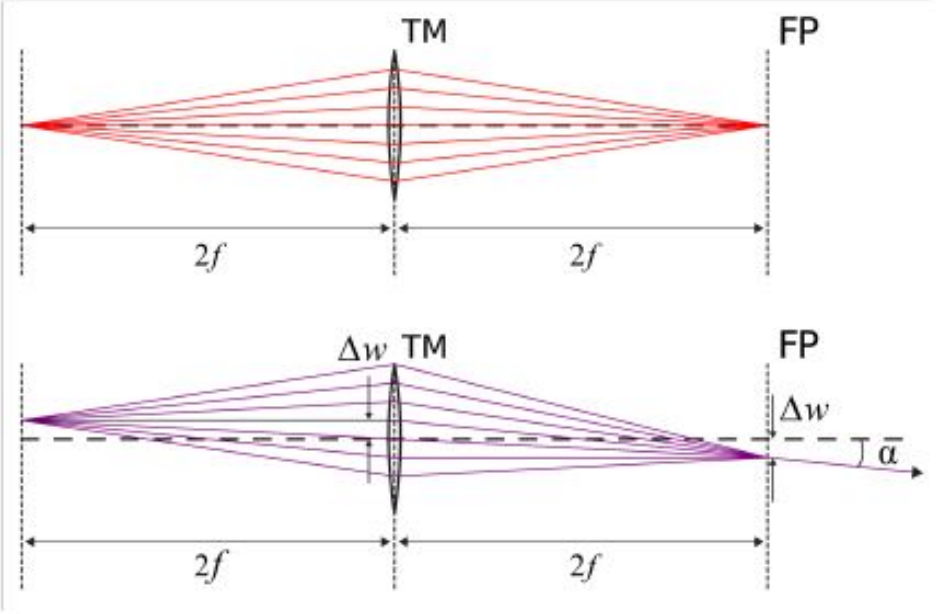

Figure 3.4: Beam walk-off caused by grazing-incidence geometry. The toroidal mirror shown as a lens with 1:1 imaging geometry. The displacement of the focal spot in the imaging plane of the setup. The wave front is tilted by an angle $\alpha = arctan(\delta w/f)$, where f is the focal length. Taken from [16]

displacement is given by the mirror movement d and grazing incidence angle Θ

$$\delta w = d \cdot \frac{sin2\Theta}{sin\Theta} \tag{3.1}$$

Displacement implies that the geometrical overlap between the two beams' foci is being decreased for increasing time delay. This is the reason why we have a limited

working time-delay range. There is also a wave front tilt, which implies a different angle of incidence on the grating surface. The displacement can be compensated by cell tracking, where the target cell position is changed by $(1.0 \pm 0.1)\mu m$ with respect to 1 fs time delay step. This value matches the theoretically calculated walk-off value, where for $\Delta\tau = 1$fs a transversal beam displacement of $\Delta w = 1.13\mu m$. More is explained in [17].
Beam alignment is a very important step in the measurement procedure. It is done with a He-Ne laser at first, and then with the driving laser. The HHG cell and filter(see below) are moved out of the way. The spherical mirror in front of the entrance to the HHG chamber and the toroidal mirror are adjusted for alignment. There is a picomotor for precision movement of the toroidal mirror. The beam is coupled out of the chamber by a mirror placed after the filter, to an improvised screen where one can see the beam cross section and the shadow of the inner-outer mirror gap. When it comes to alignment one makes small movements until the inner mirror is lying exactly at center of the beam cross section for all iris positions. This takes a lot of tweaking back and forth, of the two adjustable mirrors.

3.3 Kapton-aluminum filter characterization

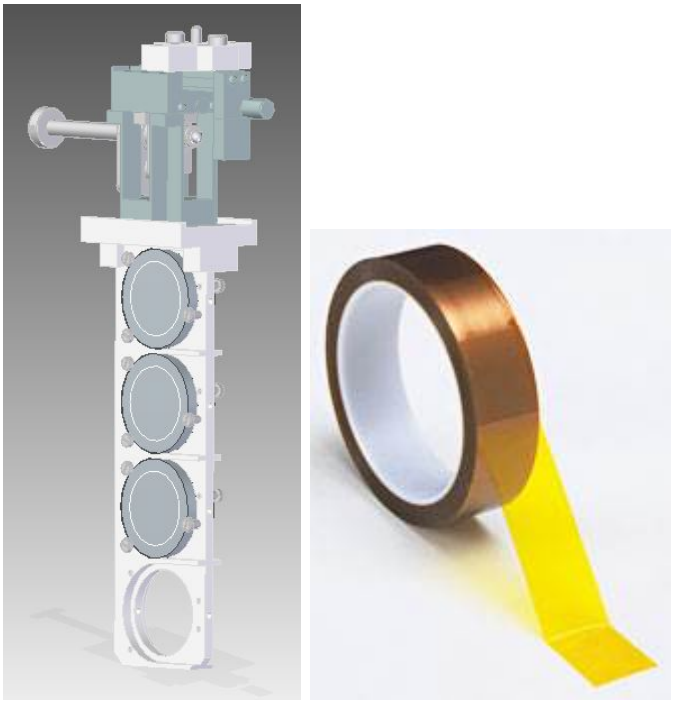

Figure 3.5: a)3D model of the new filter design, b)yellow transparent kapton tape from [18]

The old filter design consisted of a filter made of nitrocellulose and a small central filter, where both were mounted on rings of appropriate size, coaxial and spatially separated by a few mm. The filter holder was connected to a picomotor and linear

feedthrough for movement control. In the new filter design a new material called Kapton was used in place of nitrocellulose as the pellicle which filters the XUV pulse and lets through most of the NIR pulse. It was mounted on an aluminum ring (30x40 mm inner-outer diameter) and Kapton thickness is 7.5 μm. A 200 nm thick, 2 mm diameter aluminum filter which filters the NIR and lets through the XUV pulse was mounted directly onto Kapton, coaxially in the center. This configuration is an upgrade since it is a one-plane filter and no hole needed to be drilled in the pellicle with a Q-tip, like before, and there are no beam diffraction effects on an obstacle which used to be the small ring in the center. Also, a new linear drive was bought and a filter holder designed. The drive now has a longer 150 mm range and the filter holder has been made in a way to ease the handling of it in a chamber filled with mirrors and cables. The holder supports four filters, vertically aligned. The filter assembly can move along there axes for the purpose of alignment.

The role of the filter is to spatially separate the XUV and NIR laser pulses in order to have them time-delayed one with respect to the other, where the time delay is introduced by a split mirror right before the filter. The inner mirror movement delays the central part of the beams by introducing a longer or shorter beam path. The part of NIR beam from the inner mirror and the part of the XUV beam from the outer mirror are to be absorbed by the two-filter configuration. The end result is spatially separated time-delayed beams. The filter is aligned after beam alignment, by looking at the XUV spectrum on the camera, with the most counts, which means that the most intense part of the XUV pulse reflected from the inner mirror is coming through the aluminum filter. The 2 mm diameter of the aluminum filter is the same as the diameter of the inner mirror, and the two are nearly equidistant to the toroidal mirror. One can couple the beam out of the chamber on a screen where one can observe the beam size and the shadow of the inner-outer mirror gap and the aluminum filter. The filter is seen to completely cover the gap, which is exactly what is needed for separating the light coming from the inner and outer mirror. After going through the filter the beams keep converging to the same line with both foci being inside the target cell. There is a known defect of the very thin and fragile aluminum filter, called leakage, where little NIR light is going through the filter due to micro-holes in it, which deteriorate with time. This is certainly not negligible, which will be shown in the measurement data. There is also a possibility of a small misalignment of the filter, which leads to the same effect as leakage, since the NIR coming from the inner mirror is being transmitted through Kapton.

Kapton is a tough polyimide film withstanding temperatures up to 400C, with widespread applications. The properties of our interest are transmission and dispersion of the material. The experimentally calculated refractive index and absorbance curves are shown in figure 3.6. Kapton absorbs highly below 500 nm in the optical range, and has zero transmission in the whole energy range of our XUV pulse. The transmittance is calculated by dividing the wavelength spectra from the D-scan spectrometer scanned with and without Kapton, and the value is 80-90 % for almost the whole pulse spectrum, which is sufficient. The GVD of Kapton was calculated by extracting enough x and y values of the refractive index curve (fig) and trying to reproduce the same smooth part of the curve by fitting 4th order polynomial. After

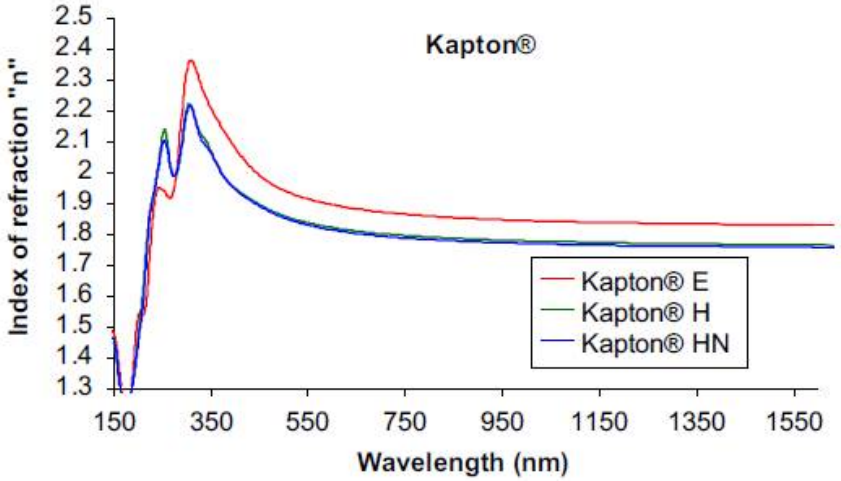

Fig. 13. Index of refraction, n, determined from ellipsometric data for polyimides.

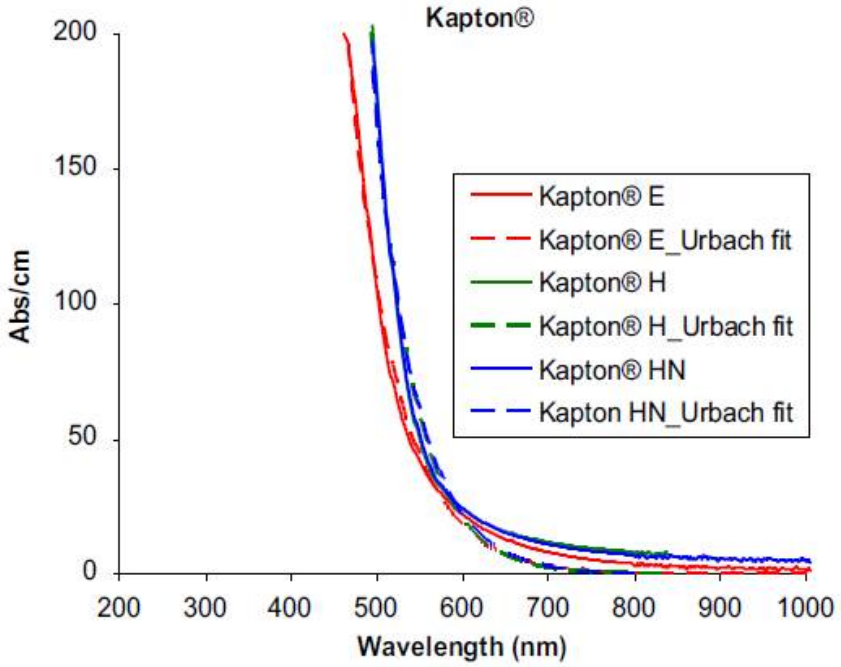

Fig. 14. Optical absorbance of polyimides.

Figure 3.6: Kapton a) refractive index and b) absorbance curves taken from [13]

getting the curve it is us in the formula:

$$GVD = \frac{\lambda^3}{2\pi c^2}\frac{d^2n}{d\lambda^2} \tag{3.2}$$

I find GVD to be 660 fs^2/mm for the central wavelength of 730 nm. In the D-scan evaluation, by Fourier transforming the spectrum from frequency domain to time domain, where we get the temporal intensity of the pulse, the pulse length was estimated by taking the FWHM of the curve. The smallest FWHM (shortest pulse)

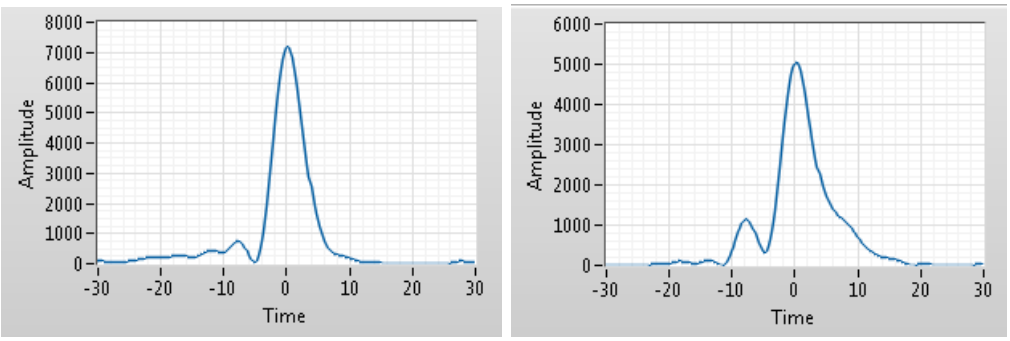

Figure 3.7: intensity profile a) without kapton and b) with kapton, retrieved from the D-scan

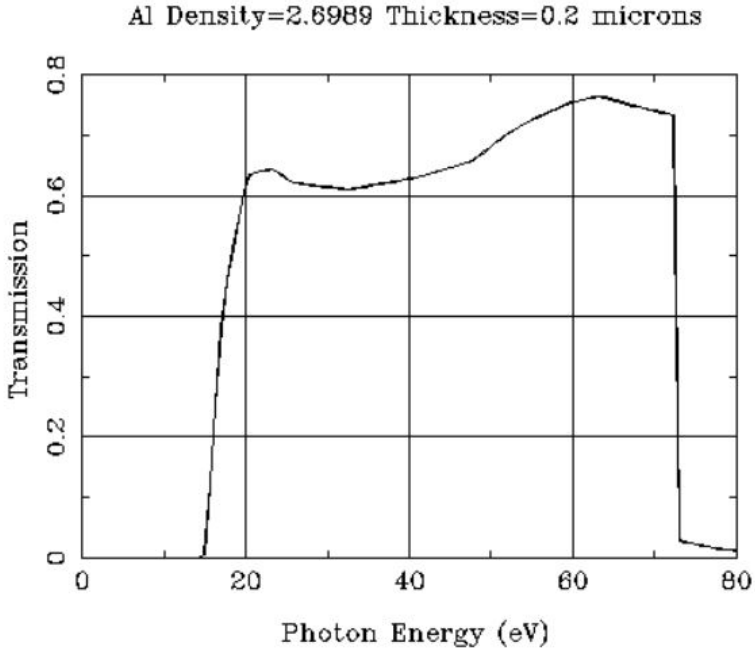

Figure 3.8: Al transmission curve, taken from [19]

was chosen from a set of FWHMs given for each wedge position, where dispersion was introduced by inserting the glass wedges in the beam path and moving them along their whole range. We used the same Kapton filter, that is a duplicate, to perform a D-scan with it. The plots in fig. 3.7 show the spectra with and without Kapton. Using the formula for the pulse length change by a dispersive material

$$\tau_{out} = \tau_{in}\sqrt{1 + \left(\frac{4ln2 \cdot GDD}{\tau_{in}^2}\right)^2} \tag{3.3}$$

which refers only to Fourier transform limited pulses and no third and higher order terms in the spectral phase Taylor expansion, I get a pulse length of $\tau_{out} = 5.65$fs for the input value of $\tau_{in} = 4.9$fs. When I compare it to the in situ estimated value

of 5.75 fs, I notice that the pulse is broadened further by higher-order dispersion of Kapton for which there's no formula to calculate the pulse duration change. The broadening also comes from the HHG nonlinear medium, where is being ionized as the harmonics are emitted, which varies the refractive index and dispersion is caused. This tells us that Kapton introduces TOD and higher orders which are significant when the pulse length approaches the optical cycle. Also the D-scan spectra confirm this, since we can see a more pronounced pre-pulse with Kapton. GVD of aluminum is negative below 50 eV, which can be used to compensate the intrinsic positive chirp of attosecond pulses. Aluminum transmission curve is given in figure 3.8.

3.4 XUV spectrometer

We own a high-resolution spectrometer for the XUV spectral range. It is a flat-field spectrograph with grazing-incidence geometry. It consists of a variable line spacing (VLS) grating. The grazing-incidence reflection grating disperses the entrance slit onto a flat spectral plane. The imaging geometry is depicted in figure 3.9. There

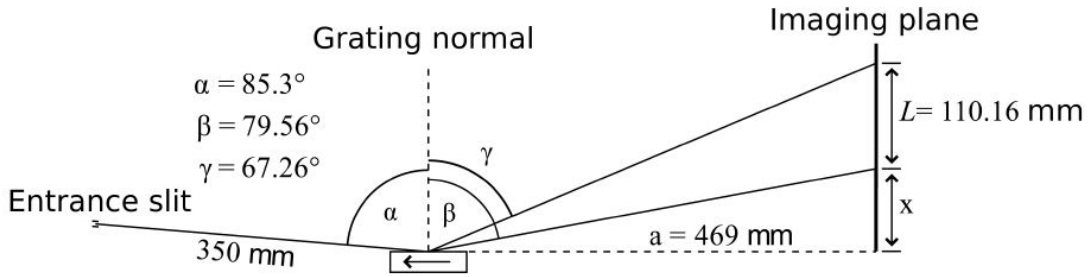

Figure 3.9: The VLS grating spectrally disperses the light from the entrance slit (target cell focal spot) onto the flat imaging plane across the distance L. The angles α, β, γ denote the angle of incidence, the maximal and the minimal angle of diffraction in the first order, respectively. Taken from [16]

are two gratings where one disperses wavelength range between 11 and 62 nm, correnssponding to 20 to 110 eV, on a flat 110 mm wide image plane, and the other one from 22 to 124 nm, corresponding to 10 to 56 eV. The XUV beam is dispersed onto a CCD camera. The camera needs to be moved along the flat spectral plane in order to encompass the whole energy range. A theoretically achievable resolution of $\sim$ 27 meV is expected assuming that the size of the camera pixel is the limiting element.

3.5 Data analysis and absorption spectroscopy

The measurement data is analyzed in the lab view program. It starts by calibrating the XUV photon energy axis. Known energies of the investigated states from

literature are used in the calibration procedure. Lines are fitted by a function corresponding to a particular line shape, which in this case was the Fano line shape. The next step in the analysis is to correct for the energy shift of absorption lines with time-delay, that is due to the beam walk-off. The time-delay axis calibration is explained in the next section, because it is done in helium, which represents one possible calibration method. The following step is the calculation of the optical density(OD) from the signal (with target gas) and reference (without target gas) spectral intensity. It is given by

$$OD(\omega) = -log_{10}\left(\frac{I_{SIG}(\omega)}{I_{REF}(\omega)}\right) = \frac{\rho \cdot z \cdot \sigma(\omega)}{ln10} \tag{3.4}$$

which is directly proportional to the single-atom absorption cross section which is proportional to the imaginary part of the refractive index , which in turn is directly related to the polarizability and thus to the frequency dependent dipole response function:

$$\sigma_{abs}(E) \propto Im(d(E)). \tag{3.5}$$

in the limit of a thin, dilute gas sample in which the absorption follows Beer's law:

$$I(\omega, z) = I_i(\omega)e^{-\rho\sigma(\omega)z} \tag{3.6}$$

where the path length-density product ρz is a measure of the optical thickness of the target gas.

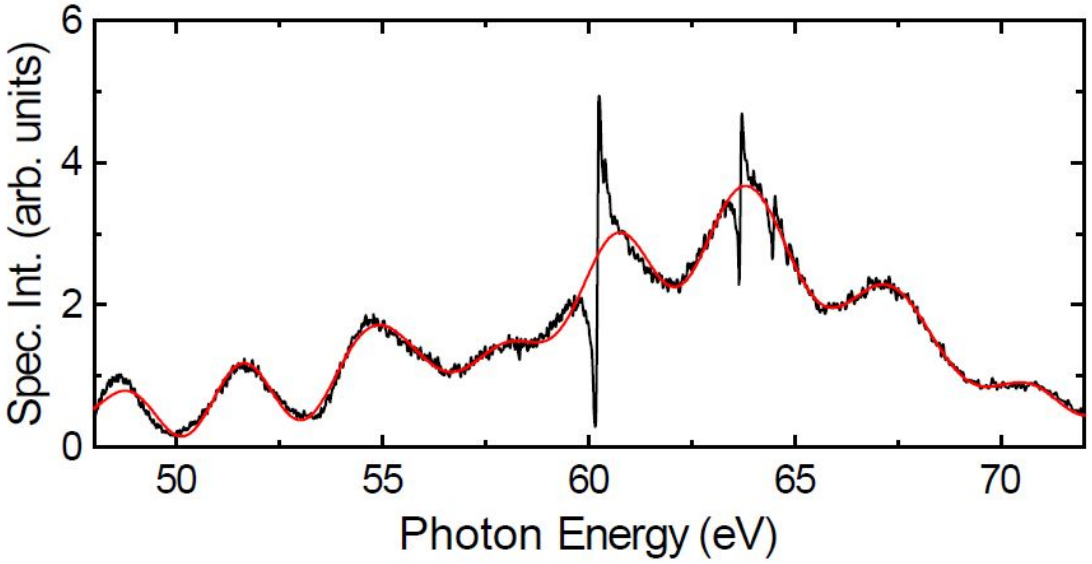

Figure 3.10: In-situ calculation of the harmonic modulation spectrum. Taken from [16]

A residual harmonic modulation is due to the intensity fluctuations of the recorded spectra with time which are due to beam pointing instabilities and the highly nonlinear harmonic generation process. To reduce the effect of fluctuations reference

spectra can be reconstructed from each obtained $I_{SIG}(\omega)$ spectrum. Using a low-pass Fourier filter, the harmonic modulation $I_f(\omega)$ can be directly retrieved from each measured signal without the sharp asymmetric absorption lines, see fig. 3.10. This $I_f(\omega)$ spectrum is scaled to obtain a reconstructed reference spectrum

$$I_{REF}(\omega) = I_f(\omega) \cdot exp[\sigma_{ABS}(\omega)\rho l] \tag{3.7}$$

with the known photo-absorption cross section in target gas. With this method the noise is significantly reduced. As the plots are insensitive to non-resonant background absorption, ΔOD is shown instead of the absolute OD.

3.6 Theory of attosecond transient absorption spectroscopy

The word transient has its definitions in the dictionary, two of which are appropriate for its meaning here: 1.passing especially quickly into and out of existence, 2. passing through or by a place with only a brief stay. The timescale of nuclear motion in molecules and phonons in solids is in the femto-to-picosecond regime. Electron dynamics are naturally happenning on a timescale ranging from tens of femtoseconds to less than an attosecond. Attosecond transient absorption (ATA) is a new technique developed to take advantage of the attosecond extreme ultraviolet (XUV) pulses to study the dynamics of the electron on its natural timescale, as well as coupled electron-nuclear dynamics. The temporal resolution is a achieved by controlling the time delay between the two ultrashort pulses and it is on the order of tens of attoseconds in our experiments, while the spectral resolution is reflected in the linewidths and other characteristic features of the recorded spectra. Paraphrasing from [11], this technique takes advantage of the inherent phase coherence between the NIR and XUV pulses that originates in the XUV generation process. "Attosecond pulses can be precisely synchronized to the electric field oscillations of an NIR probe pulse that is a time delayed clone of the strong harmonic-generating NIR pulse" (from the same source), which is achieved by phase-matching.

Our transient absorption scheme is the one where the XUV pulse initiates dynamics in the gas first, while a time-delayed few-cycle NIR pulse modifies it via coupling of the initially XUV excited bright (dipole allowed) states to nearby dark (dipole forbidden) states. This time-dependent modification results in diverse features in the absorption spectrum, some of which will be presented in this work. The XUV pulse is considered to be a weak field, while the NIR pulse is the strong field which has the ability to alter and control the electron dynamics. The polarization of both NIR and XUV is linear and pointing in the same direction. The absorption cross section is a positive quantity, but in a strong-field negative absorption may also appear, and the definition of a cross section needs to be generalized to include negative values.

Several theoretical approaches have been developed where bare-states, dressed-states and time domain pictures are used to describe differents effects and calculate the XUV absorption probability. The bare-states picture is used to describe Rabi

oscillations between strongly coupled states and to describe the perturbation of one bright state by one or more weakly coupled dark states. The dressed-states picture uses the Floquet formalism, to describe light-induced states. Everything is described in detail in [11].

Chapter 4

Intensity calibration

In this work the driving laser intensity is calibrated at the target focus position by studying the intensity dependent changes in the helium autoionizing state in the ATA spectrogram and comparing it to the simulated spectra, which I will explain in this section.

4.1 Experimental procedure and physical description

The target gas is helium, where the gas pressure is 80 mbar. The time delay range used is from -16 fs to 35 fs, where the negative time delay means that the driving laser precedes the XUV pulse. The time delay step size is 170 as. The iris position range used was from 67 to 60, with a step size of 0.5, and from 60 to 30 in steps of 5, where the iris is being opened as the numbers decrease. I will define the iris position with different numbers here. Iris position 70 (closed iris) will be 0 here, and the values increase as the iris is opened, with the same step size as in the experiment. I also want to point out that cell tracking of the walk-off has not been performed in this experiment, which may have enhanced the effect of harmonic modulations which are shown in fig. 4.1. One can especially see how the harmonics fluctuate and shift quite a bit along the energy axis. The autoionizing states of doubly-excited helium 2s2p, $sp_{2,3+}$, $sp_{2,4+}$, etc. were initially excited by the broadband XUV pulse, and subsequently coupled to other states and the continuum by the NIR pulse with controlled time delay. A level scheme of the autoionizing states is depicted in figure 4.2 I focus on the prominent 2s2p autoionizing state, first one in the Rydberg series with an energy of 60.15 eV, and linewitdh of 37 meV. An Autler-Townes splitting of this line was observed, which is a consequence of the resonant laser-coupling of the 2s2p state to the dark $2p^2$ state lying at 60.06 eV and coupling of this dark(dipole forbidden) state to the $sp_{2,3+}$ state. The line is split into a symmetric doublet, that is centered on the field-free bright state. The $sp_{2,3+}$ state shifts only slightly due to a weaker coupling to the $2p^2$ state and due to additional 2γ coupling to the 2s2p state which counteracts the $2p^2 - sp_{2,3+}$ repulsion. The larger bandwidth of the NIR

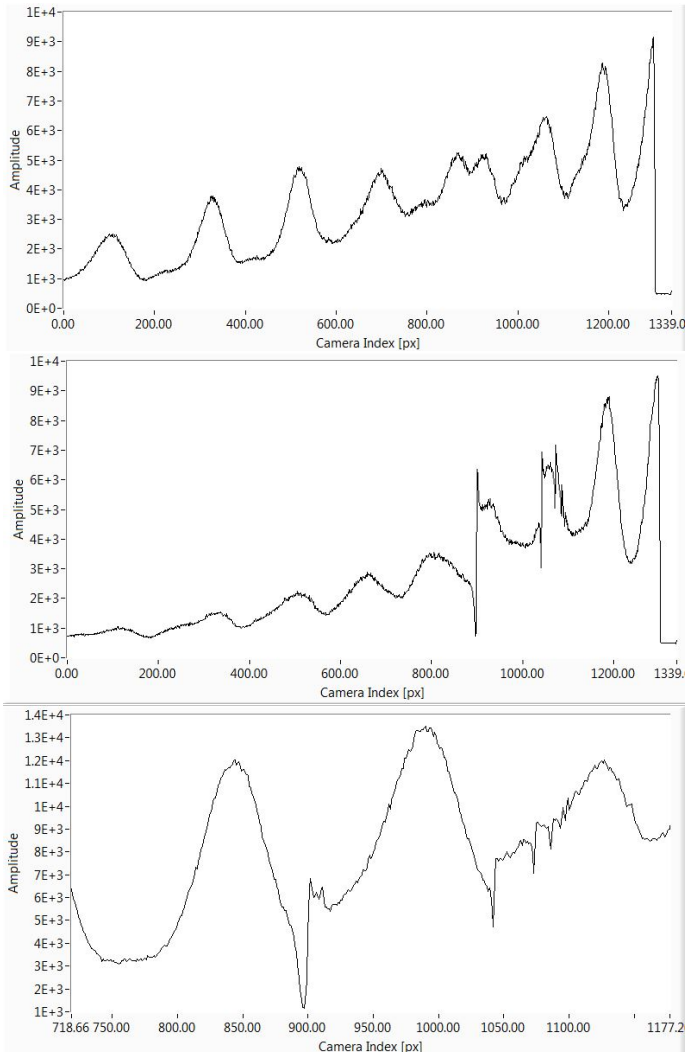

Figure 4.1: The upper plot is a raw reference spectrum taken for time delay -16 fs and and iris position 67, where an intensity fluctuation is clearly visible, and some irregular structures. The lower two plots are the corresponding raw transmitted spectra with target gas, one under the same conditions and the other for 5 fs delay and iris 65.

pulse precludes the observation of spectrally well-defined absorption lines. Maximum Autler-Townes splitting happens for a positive time delay when the initially excited states are subject to the full NIR pulse.

4.2 Estimates of the central photon energy and pulse duration at target position

Since we had a general problem of a fluctuating pulse spectrum and only approximately calibrated D-scan wavelength axis, and constant variations of pulse duration, we had to estimate the central photon energy and pulse duration at target position

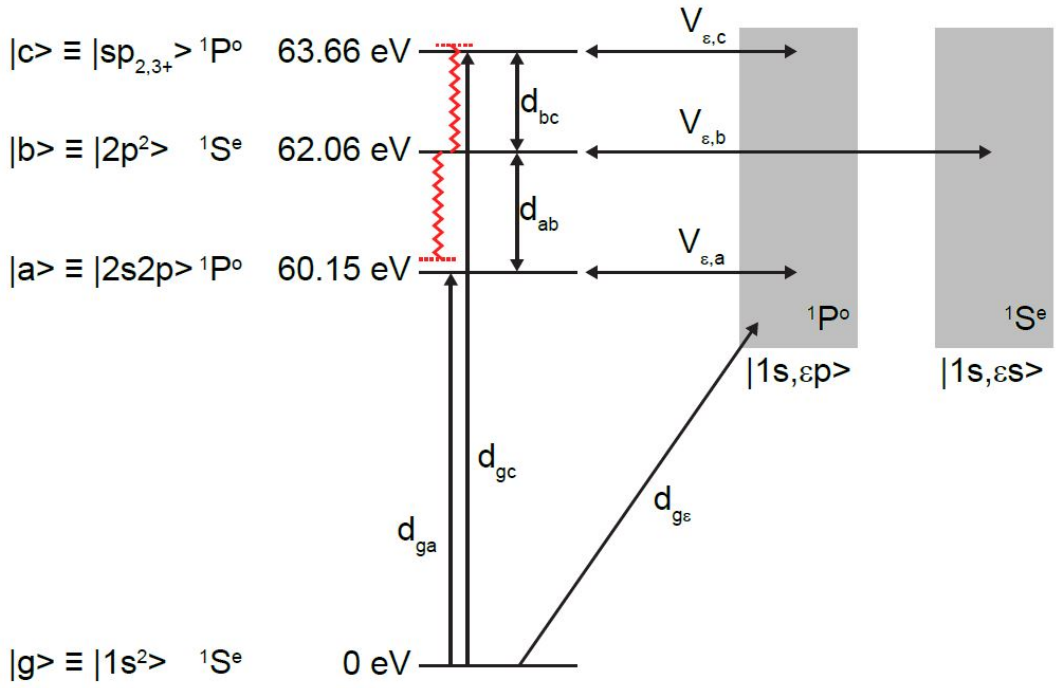

Figure 4.2: Level scheme of the simulated spectra. The ground state $|g>$, the autoionizing states $|a>, |b>, |c>$ and the continua are coupled via the dipole matrix elements d_{nm}. The configuration interaction matrix elements $V_{\varepsilon,n}$ couple the excited states with their corresponding continua. From [16]

of our driving NIR pulse . But we are still deprived of the knowledge of pulse bandwidth. It is approximately given by the D-scan spectrum to be 0.5-0.6 eV , but this is not reliable. We can perform a streaking measurement which would fully characterize both the NIR and XUV pulses, at target position. So far, only one such measurement has been performed in our lab, which didn't provide us with the parameters, but hopefully many more measurements will come and succeed.
The central photon energy of the NIR pulse is estimated by taking the energy difference between the higher-energy line of the doublet (see fig. 4.4) and the dark state which is around (1.75 ± 0.05)eV. Also the Fourier transform along the time delay axis gives Fourier energies, where there is a Fourier energy of 3.5 eV which should be twice the photon energy since the 2s2p and 2s3p states are coupled resonantly with two photons.
Pulse length at target position is different from the one measured with the D-scan due the pulse broadening by the Kapton filter, and due to some extra dispersion in the HHG medium. Therefore it needs to be estimated. For this, an in situ estimate was performed. The 2s4p excited state exhibits a ponderomotive energy shift due to the non-resonant coupling to the continuum by the NIR pulse. The acquired phase shift (given in [20]) that modifies the line shape is given by:

$$\phi_P(t,\tau) = 1/\hbar \int_0^t U_P(t'-\tau)dt' \tag{4.1}$$

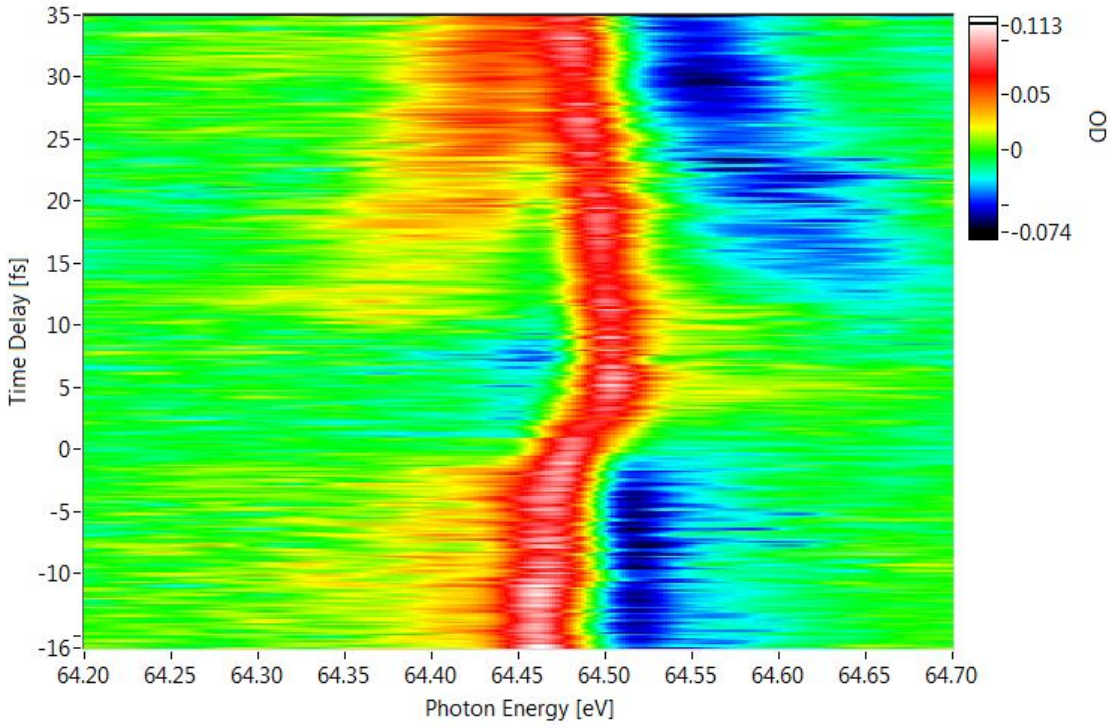

Figure 4.3: Helium doubly-excited 2s4p+ state situated at the NIR intensity $1.2 \cdot 10^{12} W/cm^2$, the ponderomotive energy shift and line shape change visible

where $U_P = \frac{I}{4\omega_0^2}$ is the ponderomotive potential, I is laser intensity and ω_0 is the central laser frequency. We use the dipole control model which says the full phase shift occurs at the instance of the interaction τ. Figure 4.3 shows the TD scan of the measured absorption spectrum of the $sp_{2,4+}$. At the energy above 64.4 eV, this state is close to the $2s^1/2p^1$ ionization threshold of helium, and it's strongly affected by the NIR dressing field. The lifetime of the state is about 190 fs, much longer than the expected pulse duration, which renders the dipole control model applicable. The lineout is fitted by the imaginary part of Dipole response function:

$$D_\tau(\omega,\tau) \propto \begin{cases} \dfrac{1 - e^{i(\omega_r-\omega)\tau-\Gamma/2\tau}(1-e^{i\phi(\tau)})}{\omega_r - \omega + i\Gamma/2} e^{i\phi_0}, \tau > 0 \\ \dfrac{e^{i\phi(\tau)}}{\omega_r - \omega + i\Gamma/2} e^{i\phi_0}, \tau < 0 \end{cases} \tag{4.2}$$

The experimental spectrum is shown in the figure. One can fit the phase by an integrated $sech^2$ temporal profile, which fits the data better than the standard Gaussian. This corresponds to a laser with a FWHM pulse duration of 5.75 fs.

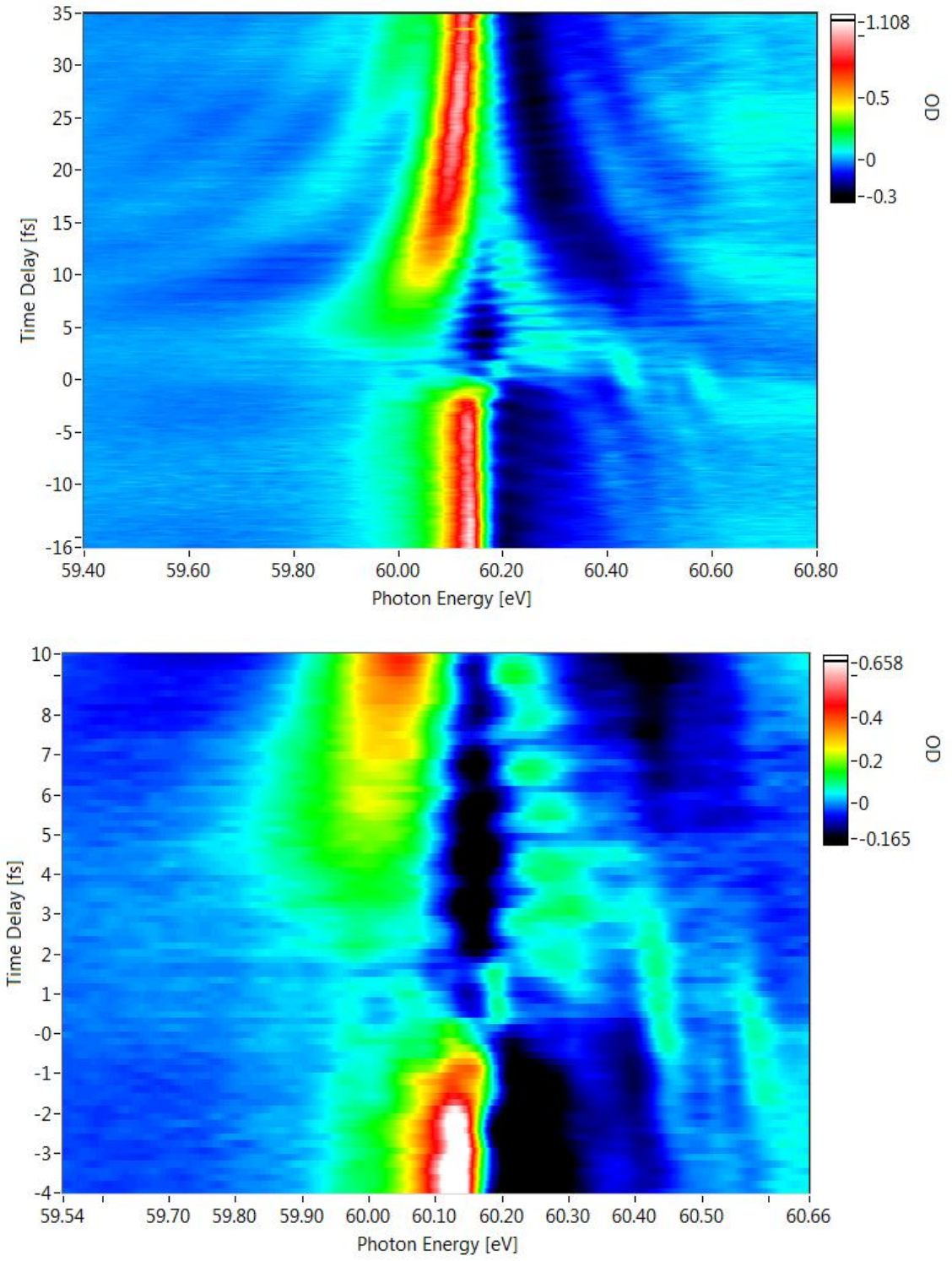

Figure 4.4: Symmetric Autler-Townes splitting of 2s2p doubly-excited state visible in the time delay scan at $1.2 \cdot 10^{12} W/cm^2$ intensity. Largest splitting happens for a time delay of 5 fs. More clearly visible in the zoomed in graph.

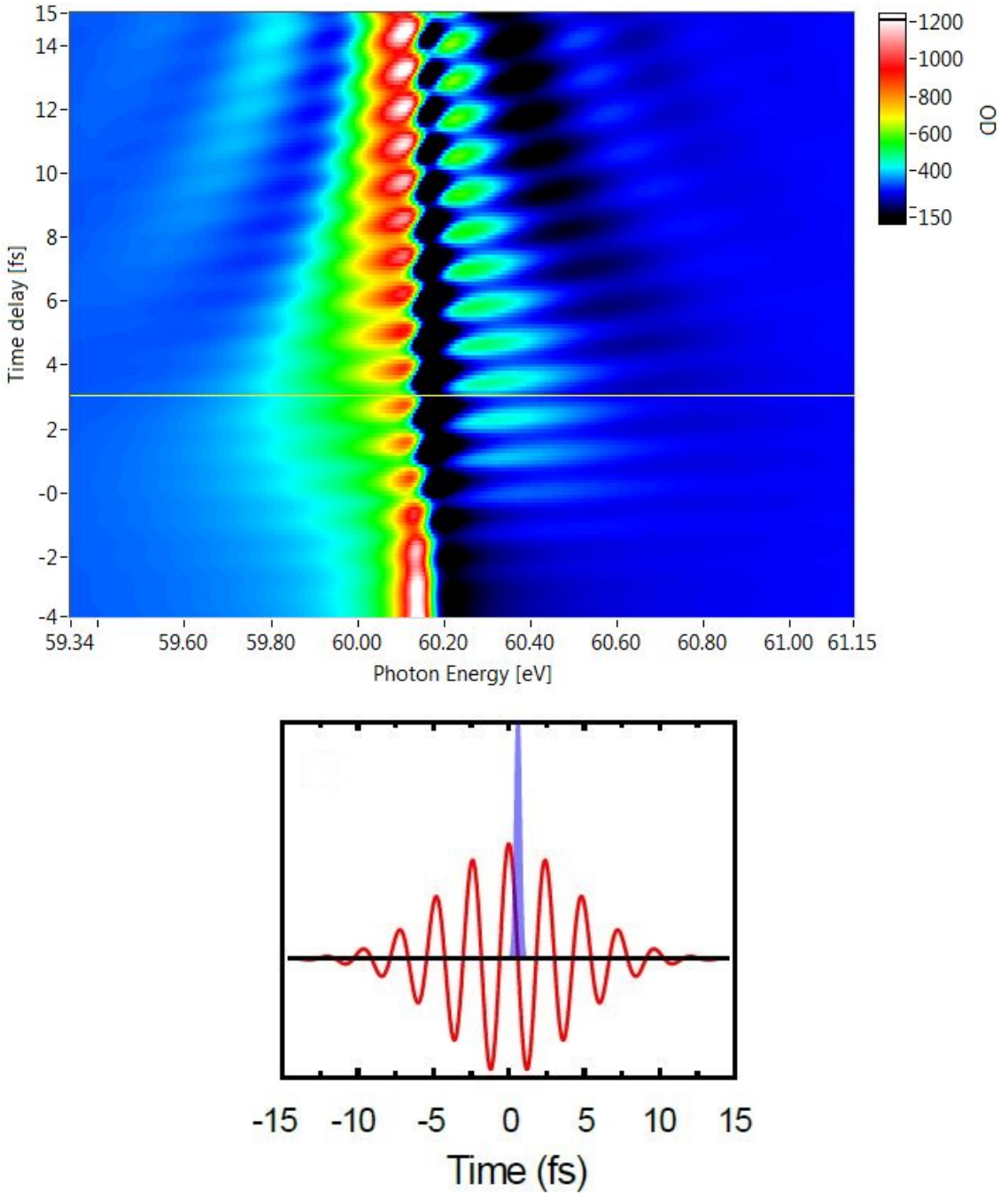

Figure 4.5: Simulated TD scan of absorption spectra for the 2s2p state with central photon energy 1.7 eV, zoomed in to more easily spot the 3 fs time delay for the largest Autler-Townes splitting. The peak intensity here is $2.25 \cdot 10^{12} W/cm^2$. The CEP was set to zero and the spectra are convolved with the experimental detector resolution.

4.3 Comparison of simulated and experimental spectra

Numerical simulations were performed using a few-level model calculation. The simulation is based on the coupling of four discrete states and their coupling to

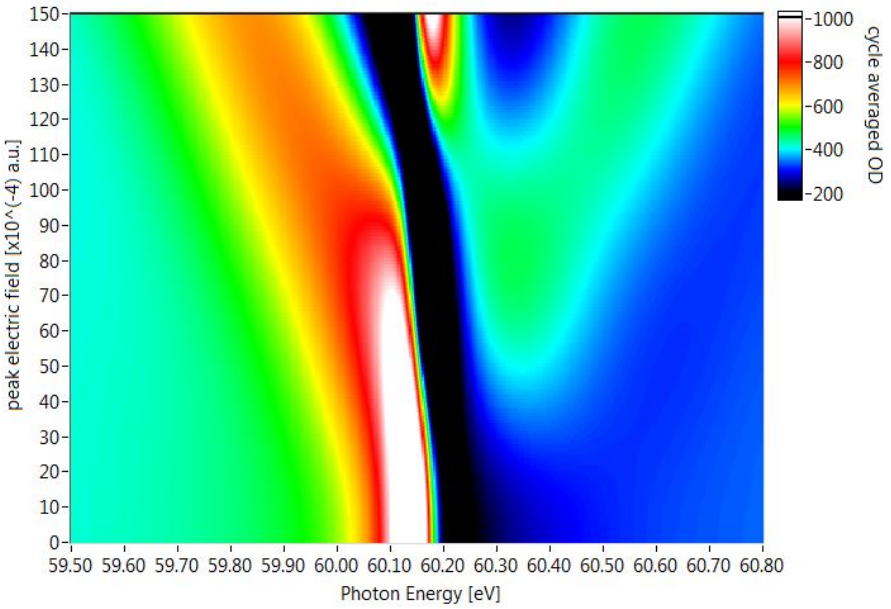

Figure 4.6: Simulated intensity scan for the 2s2p state with 1.7 eV NIR photon energy and 5.75 fs pulse length , with OD cycle-averaged around time delay 3 fs.

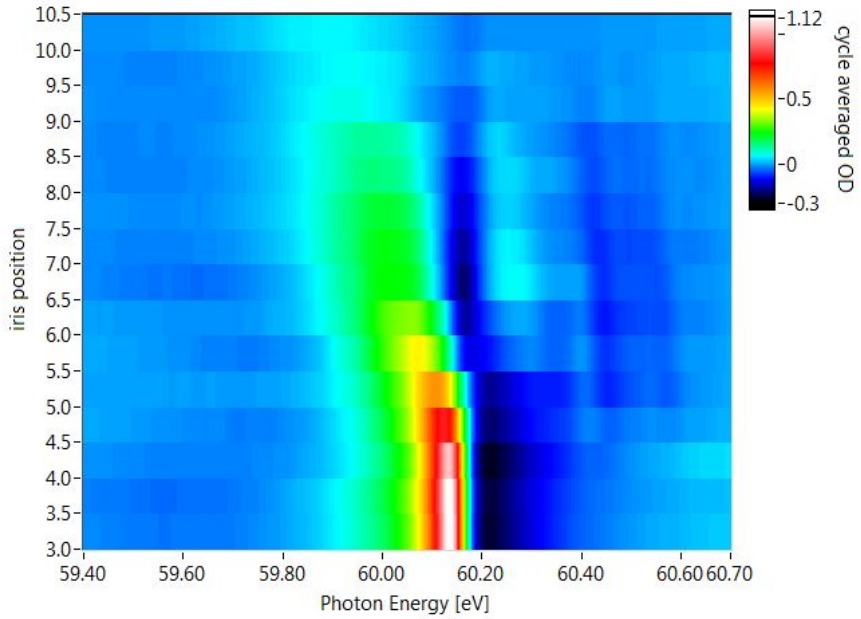

Figure 4.7: Experimental intensity scan for the 2s2p state with OD cycle-averaged around time delay 5 fs, with the iris position on the y-axis.

two autoionizing continua, where the Schrdinger equation is solved. The coupling scheme is depicted in fig. 4.2.

The laser-induced couplings between each discrete state and the other respective continuum is neglected. In the simulations two different pulse energies were used, i.e. 1.7 eV and 1.75 eV, to account for its uncertainty, and the estimated pulse length.

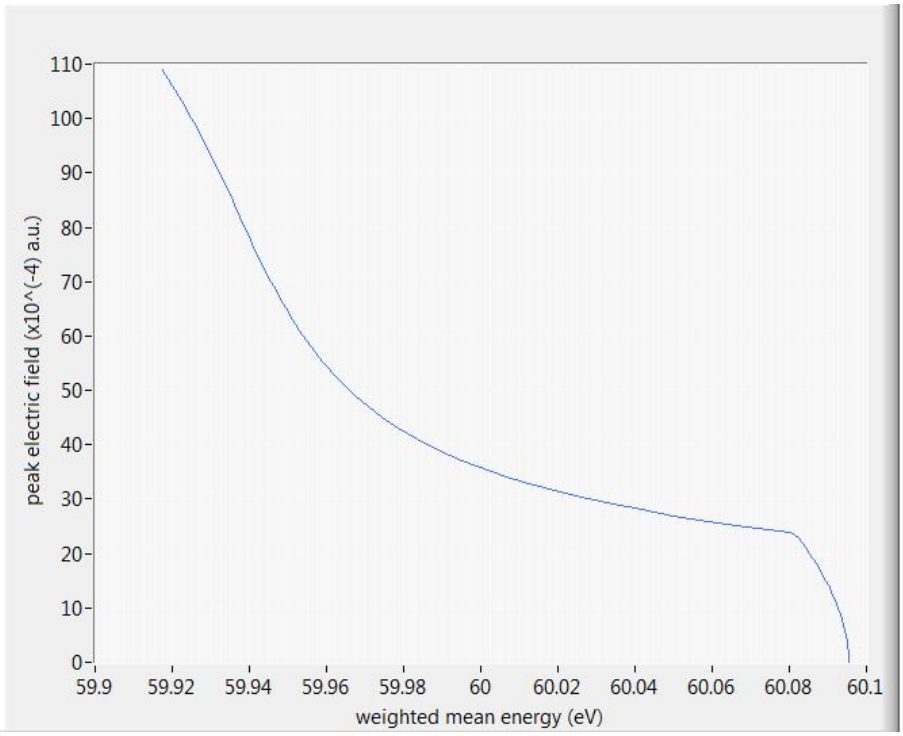

Figure 4.8: Peak electric field plotted as a function of weighted mean photon energy.

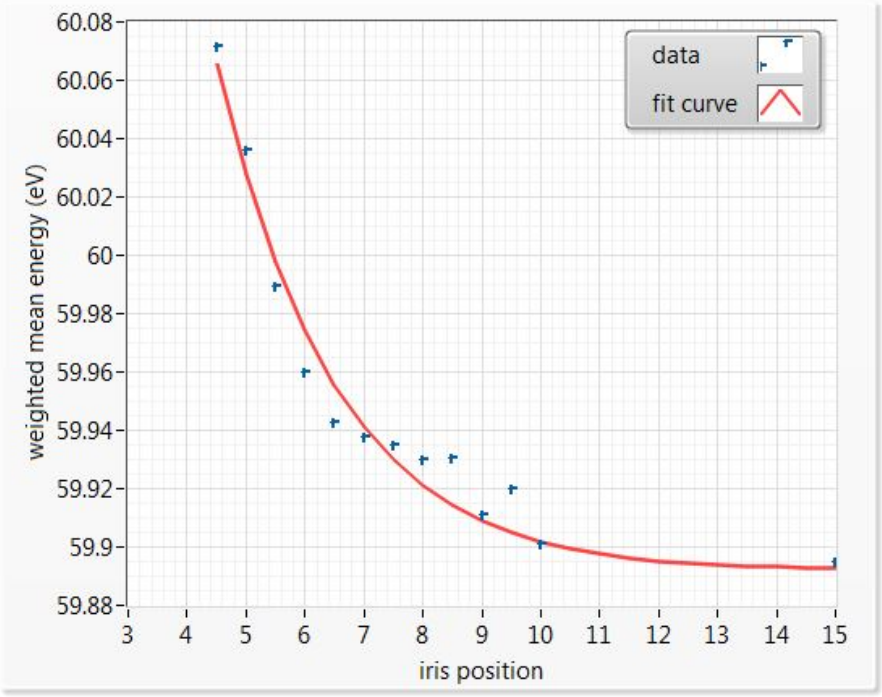

Figure 4.9: Iris position as a function of weighted mean photon energy.

Time delay for maximum Autler-Townes splitting was taken from a simulated time delay (TD) scan, and the value is roughly 3 fs, for both simulations 4.5 The OD was cycle-averaged over 2.6 fs (one optical cycle of the driving pulse) centered around the 3 fs time delay, and it was convolved with a Gaussian function whose width is roughly the camera resolution in the experiment, which is about 40 meV in the observed energy range. On a side note, time delay zero is defined as the configuration where the most intense XUV pulse coincides with the first zero-crossing after the most intense half-cycle of the NIR pulse (see fig. 4.5). In the experiment it was set by taking roughly the same position as in the simulated TD scan by looking at the line modulations.

The next step is to compare the simulated and experimental absorption spectra in order to calibrate the intensity. I chose to look at the 2s2p line itself as it shifts to lower energies with increasing intensity, whereas the other line of the Autler-Townes doublet ($2p^2 - \gamma$) is weaker, and unfortunately in the experiment we can't see it shift much so it had to be neglected, fig. 4.7 I tried to look at the maximum of the line, but many neighboring data points for different field strengths couldn't be resolved. That's why I decided to take the weighted mean value of energy in the energy interval from 59.7 eV to 60.18 eV, where I was able to get a proper curve, electric field strength versus weighted mean energy, fig. 4.8.

A third line appears in the spectrum at some field strength, which is lying in between the two lines of the doublet. Therefore I had to cut off the curve (fig. 4.6) where this line appears and then extrapolate it to higher field strengths, which is not very accurate. In the experiment the time delay for largest splitting was 5 fs, and the OD was cycle averaged around it, where the experimental intensity scan was retrieved. The weighted mean energies were calculated and plotted as a function of iris position, shown in fig. 4.9

4.3.1 The calibration curve

The final step is to read off a set of energy values from the plot and read off the electric field strength from the simulation plot corresponding to that set of energies. The electric field strength (in atomic units) is squared and multiplied by a factor $3.509 \cdot 10^{16} W/cm^2$ to get the peak intensity in SI units. The final plot is intensity versus iris position, shown in figure 4.10 The fit seems to work well in the steep area of the curve, but for iris positions smaller than 4 and greater than 12 the fit is not reliable. In the end I chose the red curve corresponding to 1.7 eV photon energy.

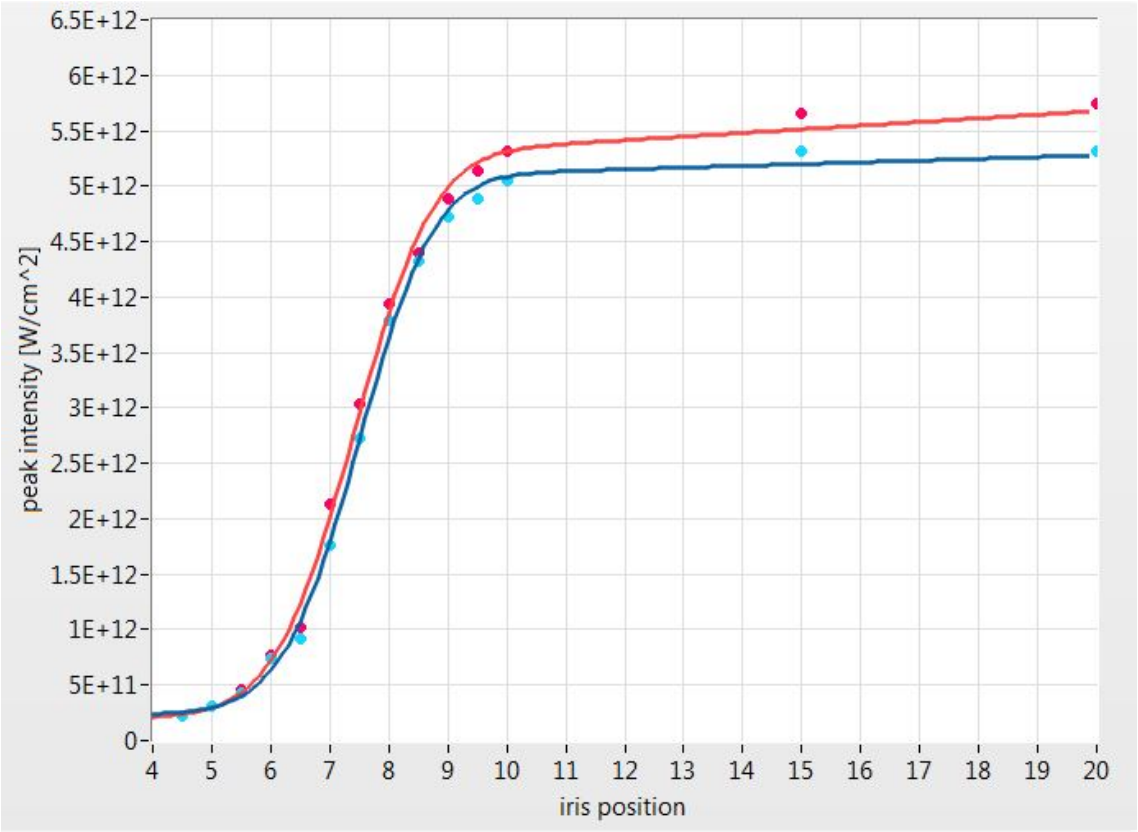

Figure 4.10: NIR peak intensity as a function of iris position, calculated using 2 simulated photon energies with 1.7 eV (red line) and 1.75 eV (blue line). The fits (solid lines) are shown together with data points.

Chapter 5

Argon measurement

This is the main part of my work, and it is about investigating the autoionizing states of argon, called window resonances, by attosecond transient absorption.

Argon is a noble gas which was discovered in 1894 by Lord Rayleigh and Sir William Ramsay. Argon makes up 0.94% of the Earth's atmosphere and is the third most abundant atmospheric gas. The electron configuration of argon is $1s^2 2s^2 2p^6 3s^2 3p^6$, with 18 electrons in total. Its atomic radius is about 20 nm. The ionization energy of argon is 15.76 eV, and of A_r^+ is 27.63 eV.

The motivation for choosing argon window resonances is due to the fact that these states have only been investigated once with this technique, since the attention was turned to principally helium and other rare gases and molecules. I already introduced window resonances in the section on autoionization, and now I'll talk about them in detail.

5.1 Argon window resonances

It turns out that the shapes of resonances - their line profiles and symmetries - are strongly affected by overlaps in energy with other resonances and interactions between them. A study of the line shapes is therefore a powerful method of understanding inter-channel interactions, i.e. physical processes which couple resonances to each other.

Argon autoionizing window resonances series involves excitation of an outermost inner-shell $3s$ electron to an autoionizing state. The series is denoted by $3s3p^6np(n \geq 4)$. The energy region of this Rydberg series is $25 - 29.3eV$. The resonances result from the decay of the excited discrete state $Ar^*\ 3s3p^6np$ into the continuum state $Ar^+\ 3s^2 3p^5 + e^-(\varepsilon l)$. The continuum can also be reached by direct photoionization, and the two possible paths interfere which produces the characteristic Beutler-Fano line shape, eq.2.26. Detailed measurements of the shape of this autoionizing series were done using absorption with photographic detection (Madden et al 1969, Baig and Ohno 1986), ion mass spectroscopy (Sorensen 1994) and electron impact studies (Wu et al 1995). These resonances have been calculated using many-body perturbation theory, multichannel quantum-defect theory, the R-matrix and K-matrix

methods, etc. Theory shows that the shape of the resonances is extremely sensitive to electron-electron correlations.

Measurements by ion mass spectroscopy induced by synchrotron radiation were

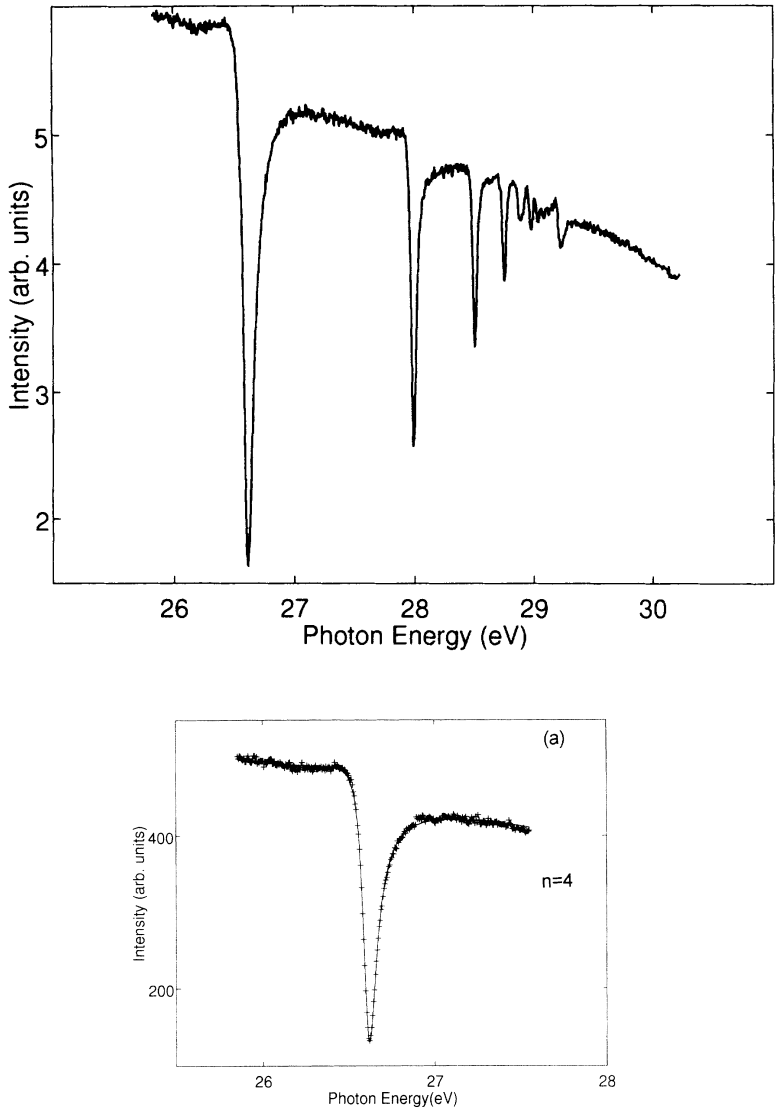

Figure 5.1: a) Ar^+ ion yield $3s^2 3p^6 \rightarrow 3s3p^6np \rightarrow 3s^2 3p^5 \varepsilon l (l = 0, 2)$ resonance series, measured with 20 meV resolution. b) n=4 resonance fitted by a convoluted Fano profile. Taken from [21].

performed in [21]. The photoion spectrum is shown in figure 5.1. It is very advantageous to be able to construct a parametrized equation which may be fitted to the measured resonances in the figure. In their case the 3s window series was fitted by a variation of the pure Fano profile which is a convolution of the Fano profile with a Lorentzian line shape, which represents the nonzero photon width of the synchrotron light. The resolution they had was 20 meV, which is the only extra parameter used for the convolution. A fitted 4p resonance is shown on the

bottom plot. It becomes more difficult to fit these curves as n increases, since instrumental effects become more pronounced as the resonance width decreases and the resonances become closer in energy. In order to give a clear representation of these resonances I have made a table of the different parameters of the states, which I have taken from [22], where there is a comparison of different measurements and calculations. I also added the dipole forbidden dark states that were excited by fast electron impact [23]. I am rounding up the values here to the second decimal. It

Window resonances:

	energy (eV)	Γ(meV)	lifetime(fs)
$3s3p^6$4p	26.61	80	8.2
$3s3p^6$5p	28	28	23.3
$3s3p^6$6p	28.51	13	52.6
$3s3p^6$7p	28.76	6.6	100
$3s3p^6$8p	28.9	4.5	146
$3s3p^6$9p	28.93	4.1	160

Dark states:

$3s3p^6$4s	25.21	202	3.25
$3s3p^6$5s	27.55	24	27
$3s3p^6$6s	28.3		
$3s3p^6$3d	27.5	<5	>130
$3s3p^6$4d	28.3	<5	>130
$3s3p^6$5d	28.63	<5	>130

Figure 5.2: Resonance energy, linewidth Γ, and the corresponding lifetime of 3s window resonances and a manifold of ns an nd dark (dipole forbidden) states in the same energy range. Taken from [22]

is also noteworthy to say that the line shape parameters of window resonances are all negative with values $q \subset (-0.1, -0.3)$, whereas q parameters of dark states have high positive values q=1.5 and $q > 10$.

5.2 Experimental procedure

Before the measurement can start, the experiment needs to be set up, starting by checking the performance of the femtosecond laser system. The next step is to look at beam cross section by a camera and determine its focus position which corresponds to the beam focused at the entrance of the hollow-core fiber. The focus position varies due to thermal effects in the femtosecond laser production, thus the laser always needs some time to warm up and stabilize, which usually takes one day. After the focus position is not fluctuating anymore, the laser is ready to go through the fiber, where a power meter is placed at the exit of the fiber. In order to get the

best fiber performance, its position needs to be tweaked with micrometer precision, where highest peak power is wanted, which is usually around 3.5 W, for the new fiber that has been installed. Right after that, a spectrometer fiber is placed at the exit of the fiber to observe the spectrum in real time. The fiber is removed and beam alignment is checked by looking at beam spot on the mirror after the fiber. Then the beam is brought to the chirped mirrors array and it goes through the wedges, and it is deflected to travel towards the D-scan spectrometer. A D-scan is performed where the retrieval algorithm shows the temporal intensity profile and best pulse duration. The next step is deflecting the beam towards the HHG chamber, where on the way an ND (neutral density) filter attenuates the beam by 3 orders of magnitude, in order prevent any damage that such a powerful laser pulse can inflict. The next thing is beam alignment which I described in the experimental setup chapter above. After that, the ND filter is removed and the HHG cell is positioned in the beam path by precision movement, where laser focus should be slightly after the HHG gas inside the cell. Harmonics were produced in argon, which was both the HHG and target gas. Vacuum inside the chambers is maintained by turbo pumps, whereas a backing pressure of 70 mbar of the HHG argon gas was adjusted to the value for best high harmonics, which can be monitored on the camera image. Also the wedges positions were adjusted for the highest number of counts. The image is that of a reference spectrum of the produced attosecond XUV pulses, so the next step is driving the target cell in both beam foci which takes place in the experimental chamber. Argon as target gas is introduced inside the cell, with a pressure of about 33 mbar, which was adjusted for the best signal. The target cell was moved to compensate for the beam walk-off. The target cell positions were adjusted for the TD scan by looking at the signal from the time delays at the boundaries and in the middle of the range, and fitting a linear curve of target position versus time delay. The final step is to put the Kapton - aluminum filter in the beam and adjust it by looking at the highest number of counts on the spectrometer, which means that the most intense central part of the XUV beam is impinging on the aluminum filter, which makes it aligned. The peaks are visible in the transmitted spectrum. The integration time was set to 3 s.

In order to start the measurement parameters need to be set up for scans. The iris position was scanned from 68 down to 58, in 0.5 steps, which translates to 2 - 12 in the new notation. This corresponds to intensities between $10^1 1$. A TD scan was done for each iris position twice for time delays between -16 fs and 52 fs, which is a range of 68 fs, where the negative time delay means that the driving laser comes before the XUV pulse. The time delay step size is 170 as, which corresponds to a mirror movement of 0.1 μm. The pulse duration from the D-scan was measured to be about 4.9 fs, which was estimated above in the helium measurement to correspond to a pulse duration of 5.75 fs at the target cell position. A pre-pulse is certainly present due to the Kapton dispersion which I evaluated in this work. The total duration of the measurement was about 17 hours.

5.3 Preliminary results of the measurement

In this section I present the evaluated preliminary results of the second measurement done on window resonances of argon in the group. The first measurement was performed by my colleague Paul Birk earlier this year, which has been only partly evaluated, which I will refer to briefly in the text.
In data analysis I had two data sets, due to the repeated TD scans. I separated them and at the end of data analysis I combined them by taking the mean value of them. I also compared all three absorption spectra, two separate and the resulting mean one, and they all seem to match more or less with no significant deviations and all the same effects are seen in every one of them. Further analysis was therefore done only with the mean absorption spectrum. Data analysis procedure is described in the section above. The raw spectrum is shown in figure 5.3. The peak of the

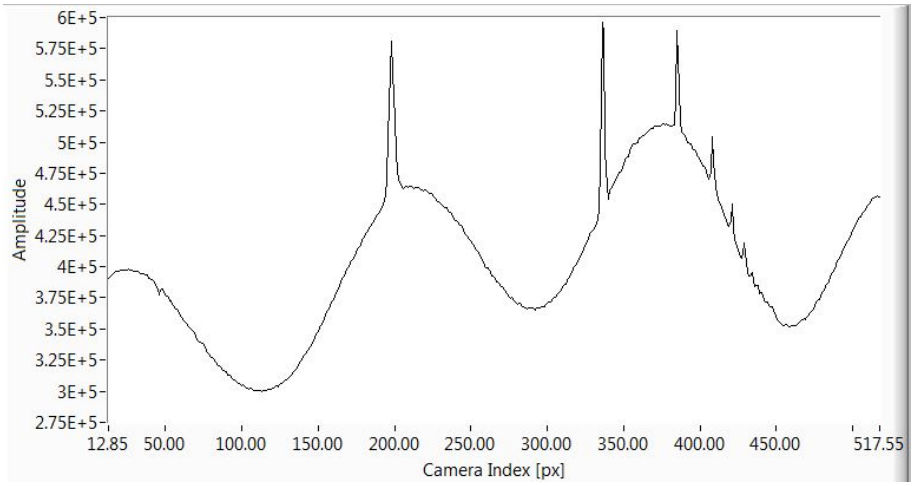

Figure 5.3: Raw transmitted XUV spectrum shown for the lowest intensity $1.5 \cdot 10^{11} W/cm^2$ and 10 fs time delay.

first resonance in the series should be large compared to the peak of the second resonance, which is seen in figure 5.1. In this measurement this is not the case, but the peaks are of similar height as shown in fig. 5.4, where for certain parameters the highest peak becomes the second one in the series. The first measurement, done earlier this year doesn't show such behavior, but a very large first peak, which should be the case. So far I haven't found a proper explanation for this, but there could be propagation effects in the medium due to pressure.
Energy axis calibration is done by taking the tabulated values of resonance energies shown in table 5.5. The peaks were fit by a Fano line profile fit function, and the grating equation for the low energy grating, which was used in the experiment, was implemented in order to complete the energy axis calibration. With the calibrated energy axis I tried to estimate the linewidth of the resonances by looking at the FWHM of the peaks. The data set for the minimum intensity was used and the most negative time delay in order to exclude the broadening of the linewidth by the NIR laser. The estimated value of the linewidth of the first resonance is around

40 meV, which is twice smaller that its known natural linewidth of 80 meV. For the second resonance the estimated linewidth is 25 meV which is still smaller that its natural 28.2 meV linewidth. In the measurement earlier this year the linewidth of the first resonance has the right value of around 80 meV, and the linewidth of the second resonance is estimated to be around 50 meV, which should represent the resolution of the grating spectrometer in this energy range. Another fact is that there are six clearly visible peaks in the spectrum, as compared to seven or even eight peaks from the earlier measurement. In the raw transmitted spectrum in figure 5.3 there are clearly visible harmonics which appear to be both even and odd harmonics, judging from the known energies of the resonances. The distance between the harmonics from the energy calibrated spectrum is found to be about 1.7 eV, i.e. one NIR photon energy. The time delay had already been calibrated

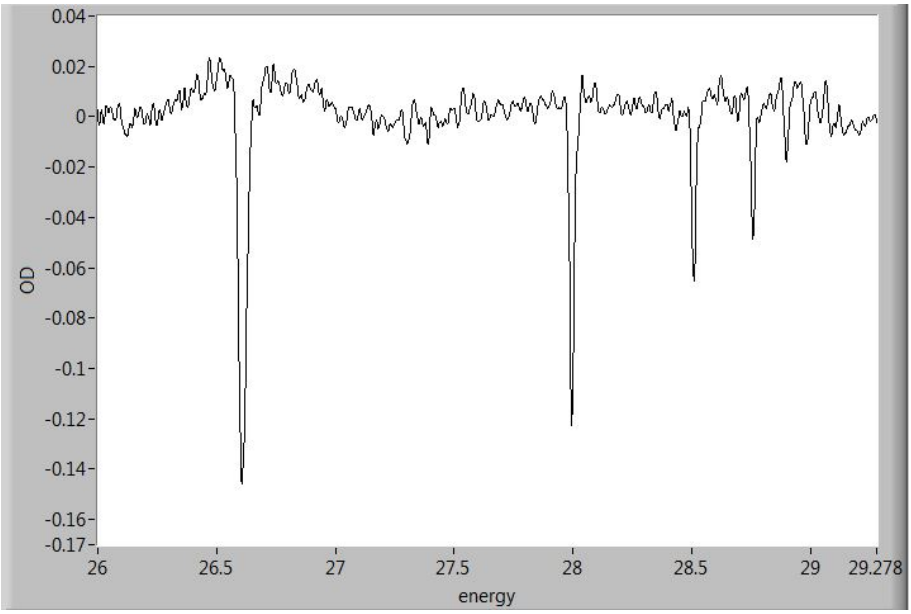

Figure 5.4: Lineout of the TD scan for a -10 fs TD for the lowest intensity used.

Series	State configuration	Energy (eV)	Decay rate (meV)
Window resonances in argon	$n = 4$	26.606	76
	$n = 5$	27.993	25
	$n = 6$	28.506	16
	$n = 7$	28.757	9
	$n = 8$	28.898	10

Figure 5.5: Energies and linewidths of window resonances taken from [21]

with helium. Corrections of skewness of the spectral lines due to walk-off were done.

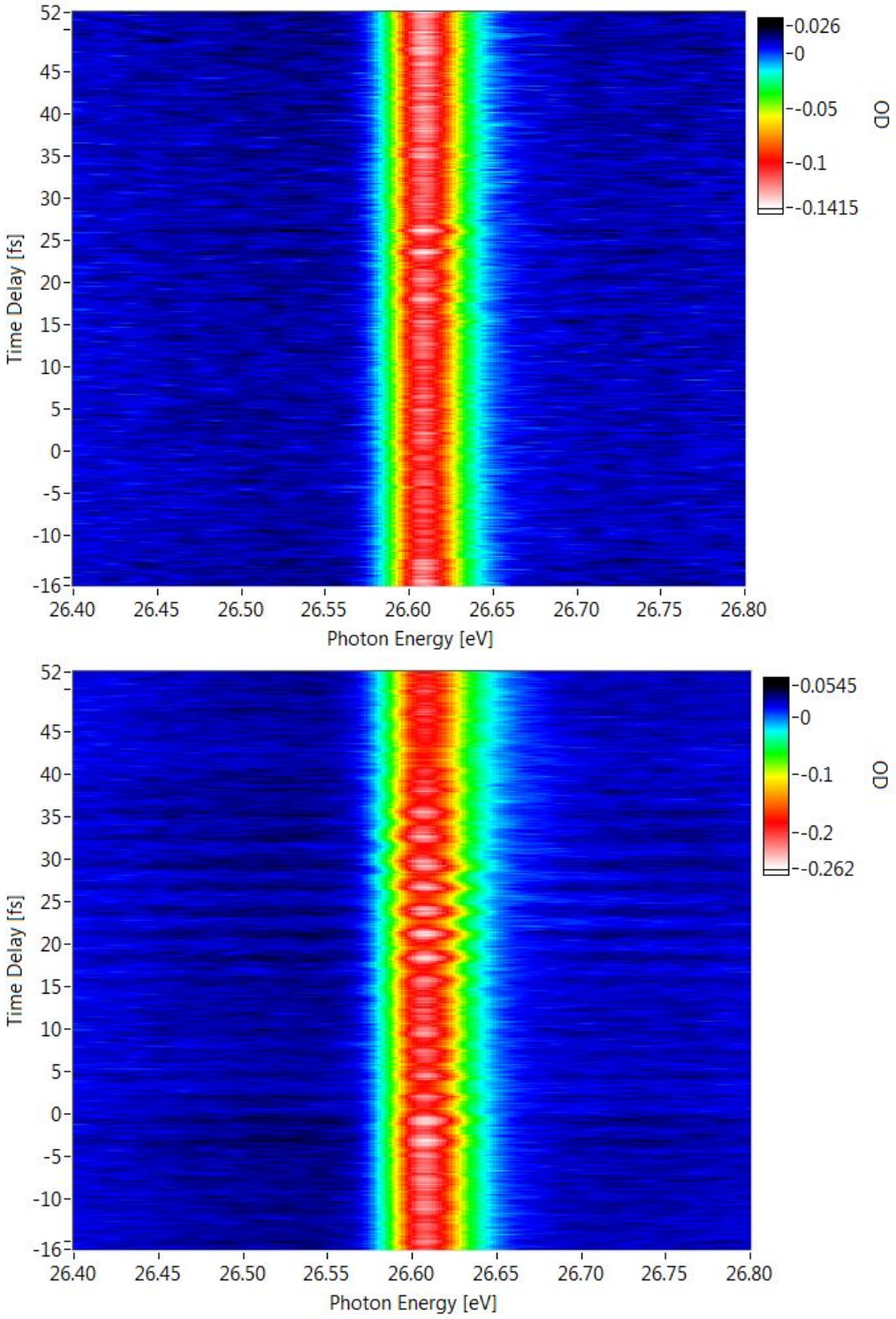

Figure 5.6: XUV absorption spectra of the lowest-lying 4p resonance at intensities $1.5 \cdot 10^{11} W/cm^2$ and $2.1 \cdot 10^{11} W/cm^2$, respectively. Negative time delays mean that the NIR pulse is arriving on the target first. Different oscillations are visible together with line broadening, shifting and splitting.

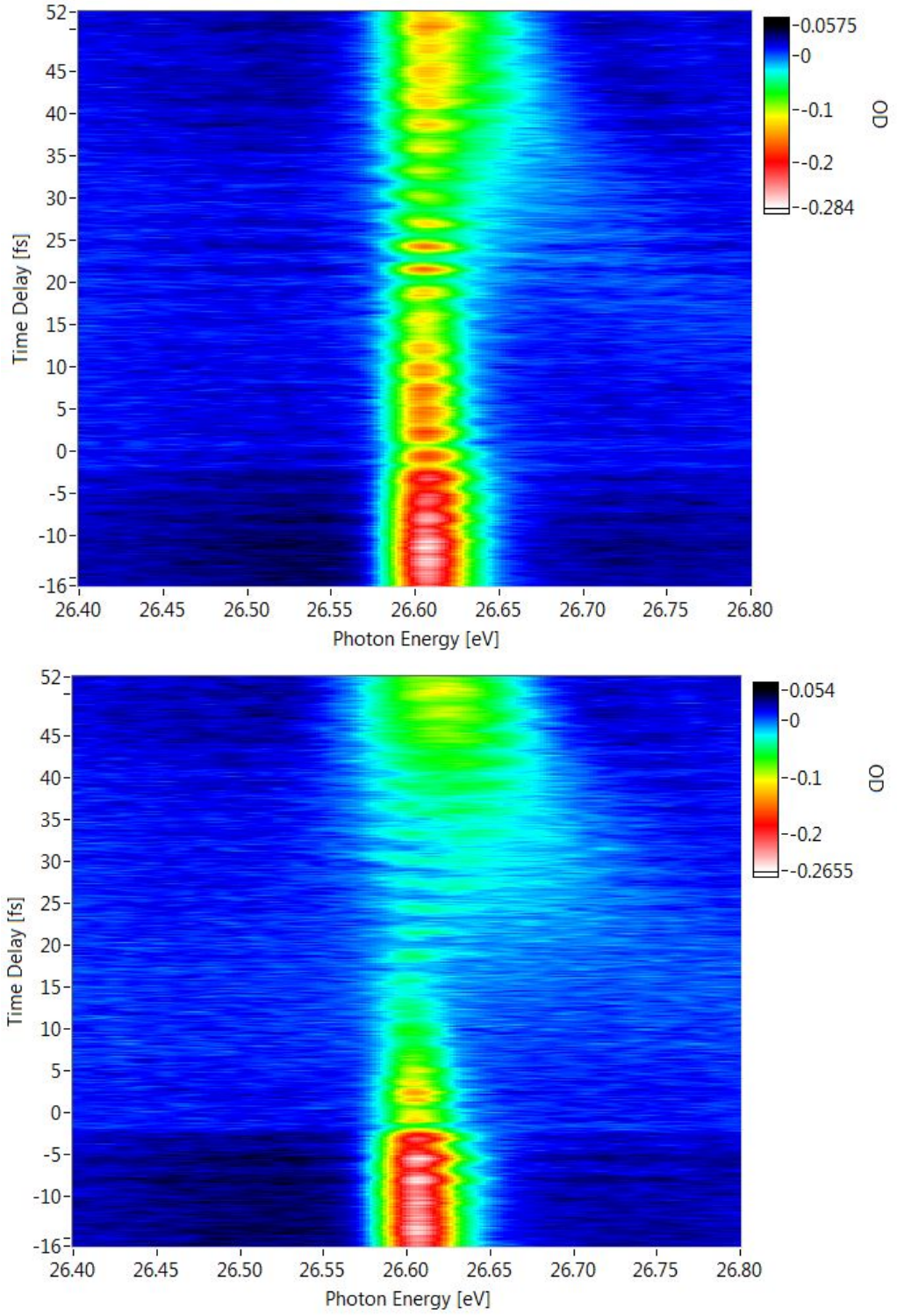

Figure 5.7: XUV absorption spectra of the same resonance at intensities $4.4 \cdot 10^{11} W/cm^2$ and $1.2 \cdot 10^{12} W/cm^2$, respectively.

It was corrected by looking at the line of the 4p state for the lowest intensity, but there is a negligible skewness left when the intensity increases. In further analysis the Fourier filtering technique is used as usual, but a disadvantage of this technique is that the absorption line profile is not preserved in the area of the outer parts of the line around zero ΔOD, which can be visible in figure 5.4.

The retrieved absorption spectra are shown in figure 5.7. If one takes a look at

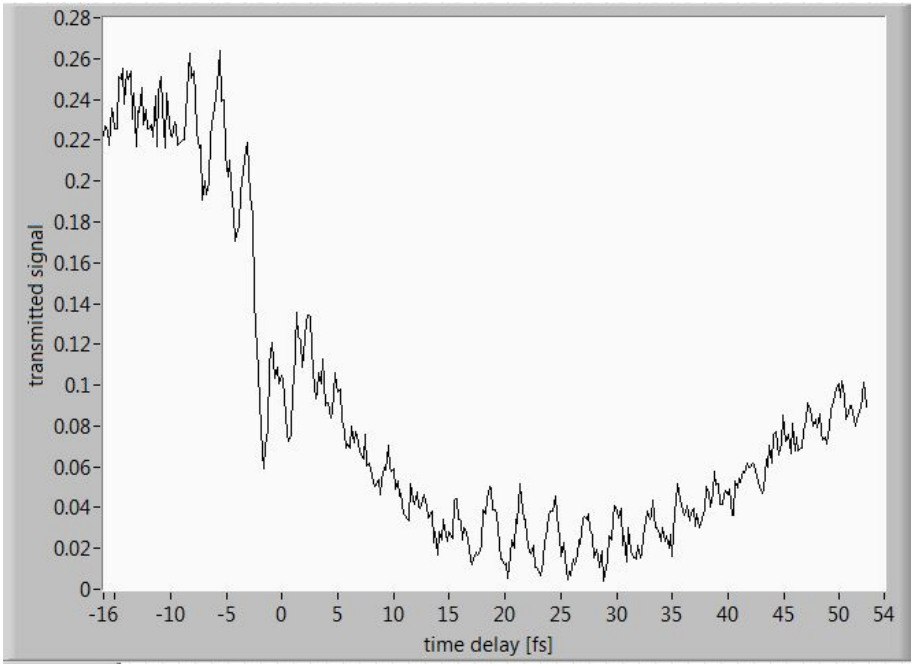

Figure 5.8: Lineout of the second graph of the previous figure at the resonance energy of 26.61 eV.

the lineout of the graphs for the negative time delays, the line is shifting slightly to lower energies as the intensity grows, where the shift is increasing as the time delay approaches zero. In the third graph the line starts shifting back and forth to a slightly lower energy simultaneously with the oscillations in OD. The line shape starts to significantly change in the third graph at around 20 fs time delay, where the line starts broadening as the time delay increases, and for largest delays its linewidth increases by about 50%. The line broadening increases with intensity. Already in the fourth graph the absorption line starts splitting at around 15 fs, where a very broad and distorted line emerges at roughly 35 fs delay. Another conspicuous feature is line weakening which is significant already in the third graph. It starts happening at a time delay of -2 fs, with the limit gradually moving towards -5 fs with increasing intensity. The signal drop due to weakening is clearly visible in a lineout at the resonance energy of the fourth graph, shown in fig. 5.8

Since oscillations of lines with changing time delay of different frequencies are present throughout the whole measurement, it is important to find out what the oscillation frequencies or Fourier energies are. Therefore, a Fourier transform is performed of the time delay axis, and part of the Fourier spectrum is shown in figure 5.9. When we are looking at the first resonance, it oscillates not only with

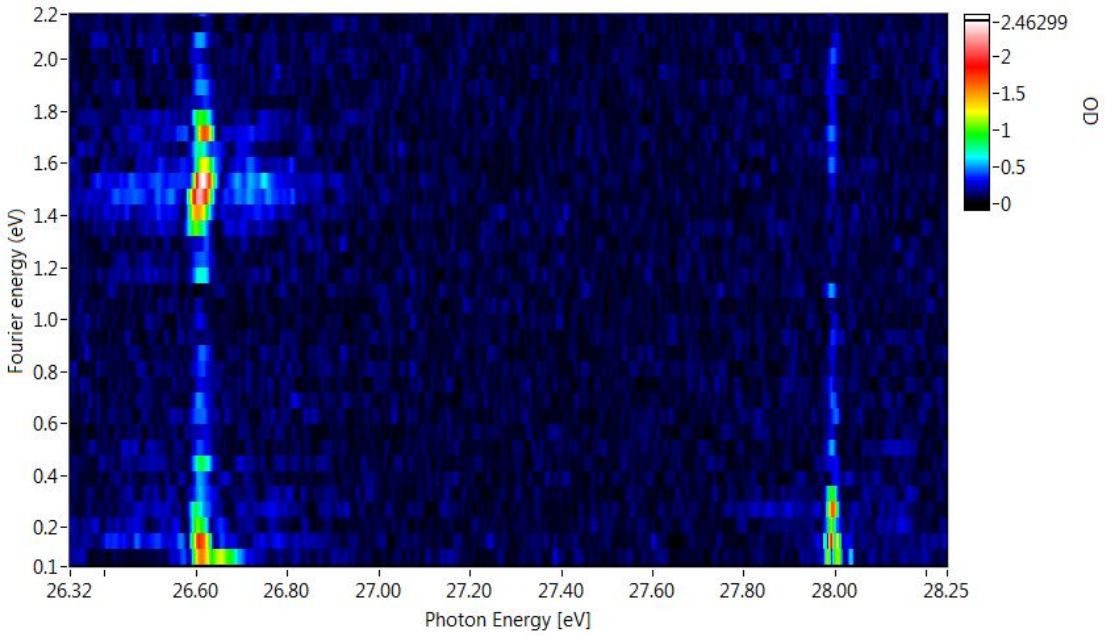

Figure 5.9: Fourier transformed spectrum of the time delay axis for the intensity of $2.1 \cdot 10^{11} W/cm^2$. Strongest oscillations appear at a Fourier energy of 1.5 and 1.7 eV, which is roughly one NIR photon energy. Slow oscillations of below 0.5 eV are also apparent. The second resonance starts oscillating more with higher intensity.

the shown Fourier energies, but also with 2.05 eV and even from 0 eV to nearly 1 eV for higher NIR intensity. These oscillations have two different origins, non-resonant coupling of states to continua and resonant coupling to other autoionizing states, with the NIR laser photons. The Fourier energy should represent the energy difference between the initial and final state in the coupling of states.
When it comes to resonant coupling, there is a manifold of dark states to which the bright states couple, whose energies are given in table 5.2. Dark state 4d is lying 1.7 eV above the 4p state and they are thus resonantly coupled. I mentioned earlier in the thesis that our aluminum filter has leakage which is causing some of the NIR light to go through it, and these photons are not time-delayed with respect to XUV photons. Therefore some dark states, both ns and nd states, are initially populated by a transition with one XUV and one NIR photon. After a time delay another NIR photon resonantly couples the 4d dark state to the 4p resonance. Also an oscillation is visible at 2.05 eV Fourier energy which suggests resonant coupling to the higher-lying 5d state which is 2.02 eV above the 4p state, with the assumption that this energy is within the NIR laser bandwidth. Since the NIR laser imposes a time and time delay dependent phase, eq. 2.28, on the dipole moment of the decaying bright state, constructive or destructive interference can be caused between the decaying dipole phase and the so-called light induced phase, which manifests itself in oscillations of the optical density as a function of time delay. The oscillations appear even at negative time delays , such as -9 fs, which may be to due a pre-pulse that is certainly present in our NIR laser, due to Kapton dispersion as shown

earlier. Therefore population transfer from one state to the other is happening,

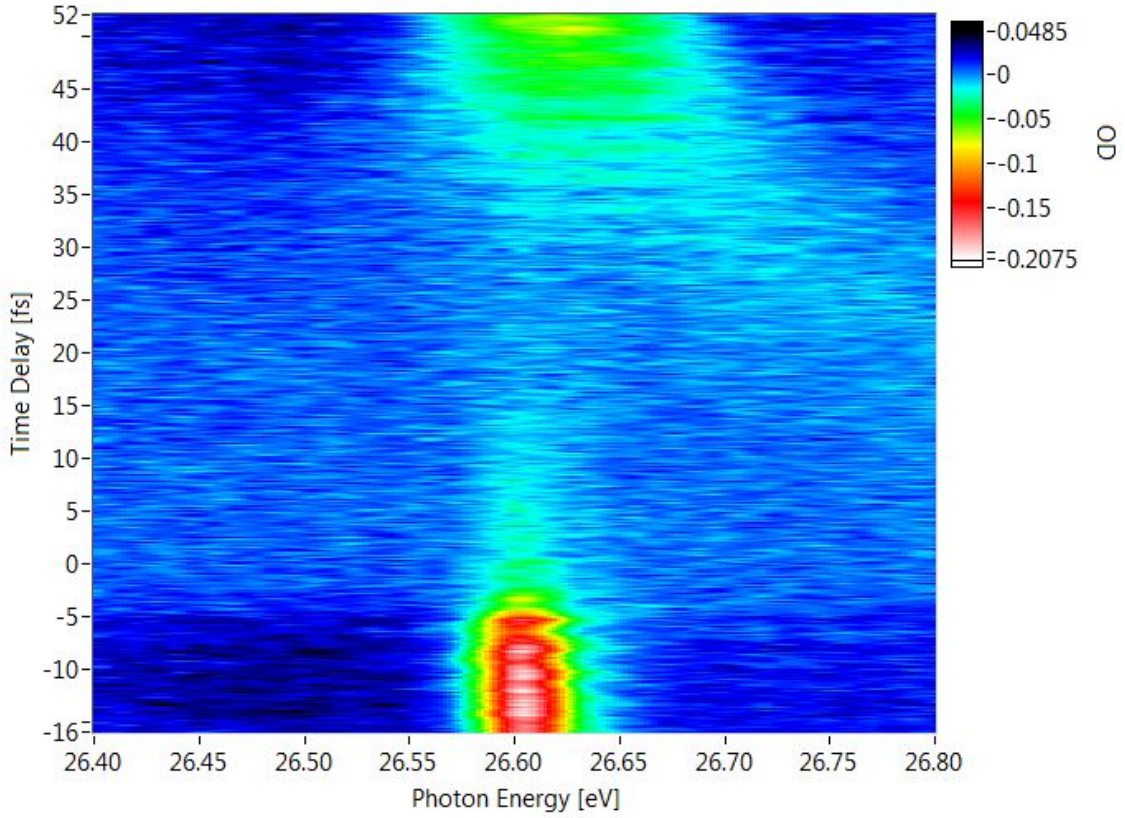

Figure 5.10: XUV absorption spectrum of the 4p resonance at intensity $5{\cdot}10^{12} W/cm^2$. The line is splitting further, and it is getting broader and weaker.

where the amplitude which quantifies the population is a function of time delay. If we try to look at other possible coupling schemes, there seems to be no possibility of a ladder, lambda or vee-type coupling of bright states given all the known states and a limited NIR bandwidth. There is always a possibility of two-photon coupling of two states (no intermediate state) that are far enough apart, which is not accounted for in the latter statement.
If we look at the slow oscillations of below 0.5 eV, they should come from Raman-like non-resonant coupling to $Ar^{*+}(3s3p^6\varepsilon l)$ continuum whose threshold is around 29.3 eV , where NIR photons of different energies participate in the coupling.
Since the 4p state is more deeply bound than the 5p and 6p states with respect to the $Ar^{*+}(3s3p^6\varepsilon l)$ continuum, coupling only to this continuum means that the 4p state should be less affected by the NIR laser, which is just the opposite in the experiment. This proves that resonant coupling to dark states is the dominant coupling mechanism.

Now, when the intensity increases the 4p state is getting ionized, where the splitting of the line starts to increase and include a larger time-delay range, seen in figure 5.10 . But, for the highest intensity used in the measurement the line appears again, but with a different line shape, which you can see in figure 5.11. The line

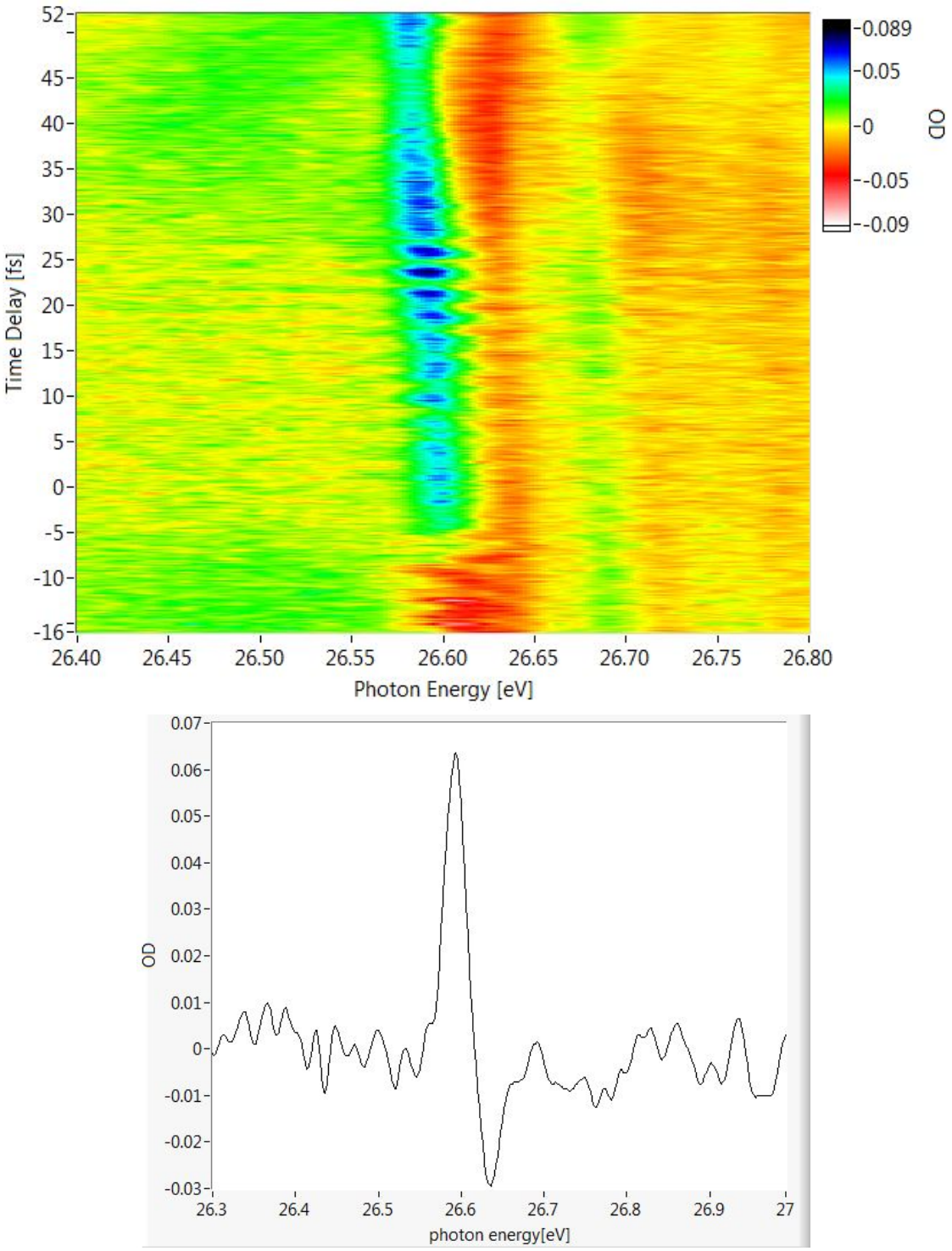

Figure 5.11: Absorption spectrum of the 4p state at the intensity of $5 \cdot 10^{12} W/cm^2$, where a change to a Fano line shape is seen. Lineout of the graph at TD=9 fs is shown below.

has a Fano line shape similar to that of the above described helium autoionizing

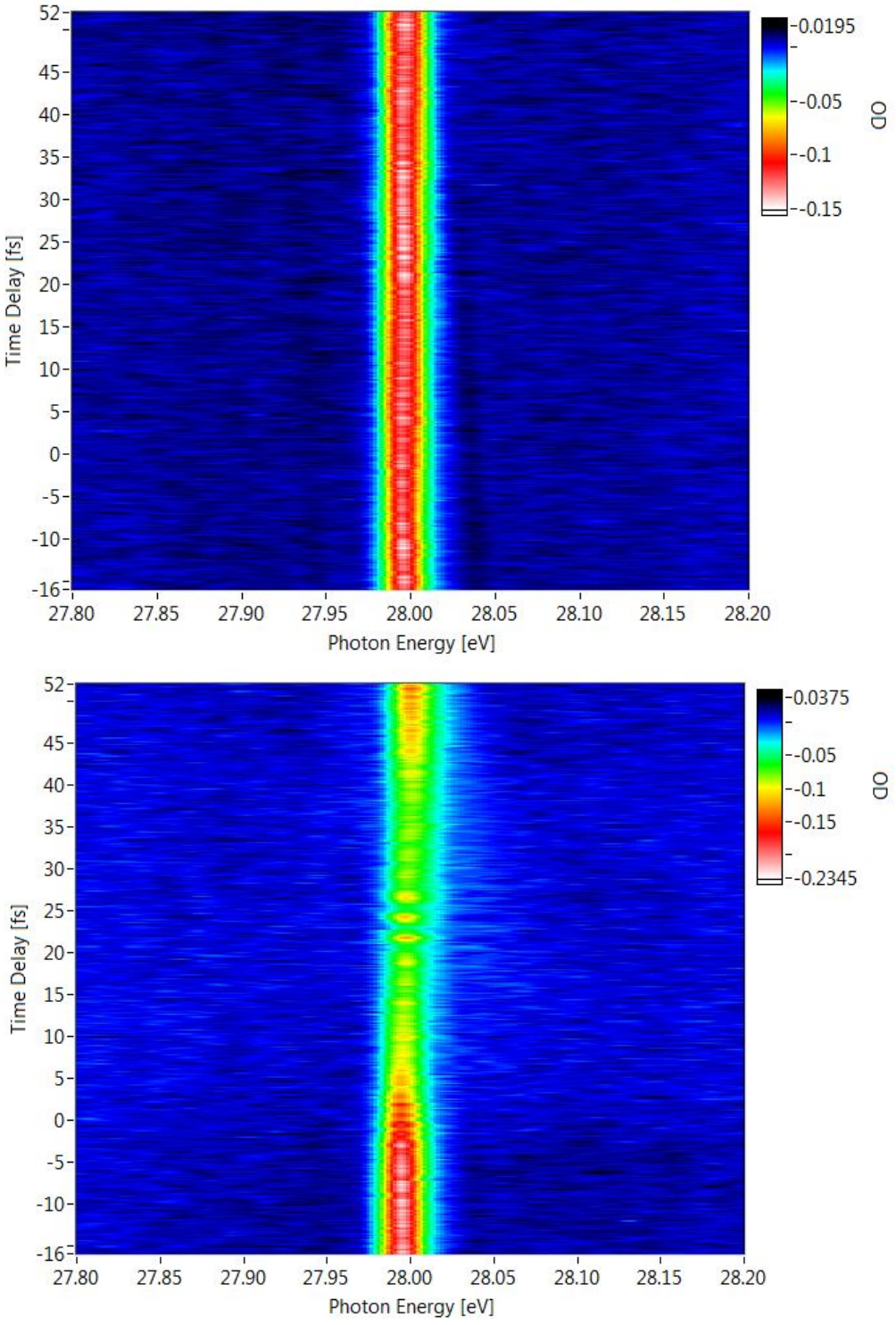

Figure 5.12: XUV absorption spectra of the second resonance state 5p at intensities $1.5 \cdot 10^{11} W/cm^2$ and $1.2 \cdot 10^{12} W/cm^2$, respectively.

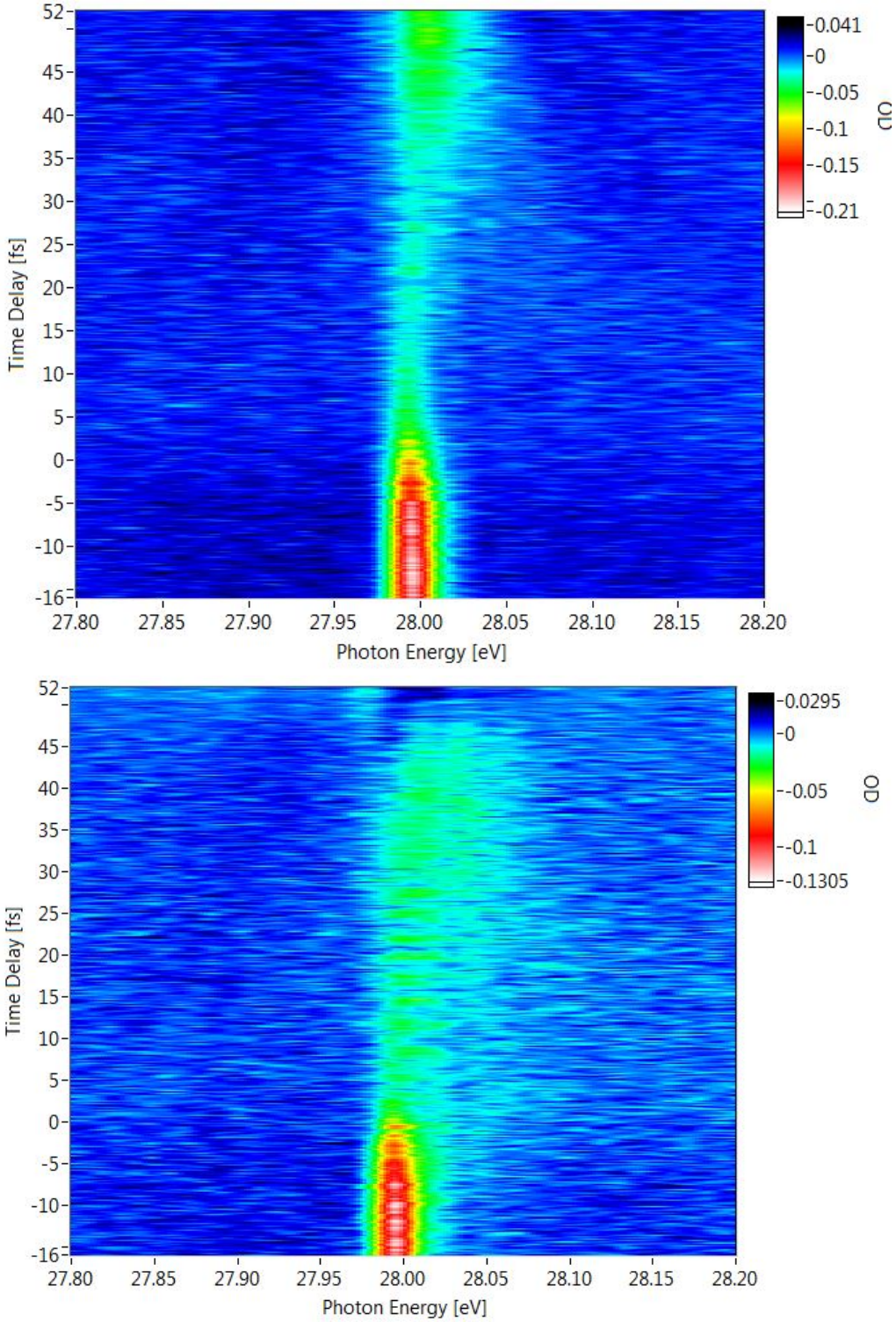

Figure 5.13: XUV absorption spectra of the same resonance at intensities $5 \cdot 10^{12} W/cm^2$ and $5.4 \cdot 10^{12} W/cm^2$, respectively.

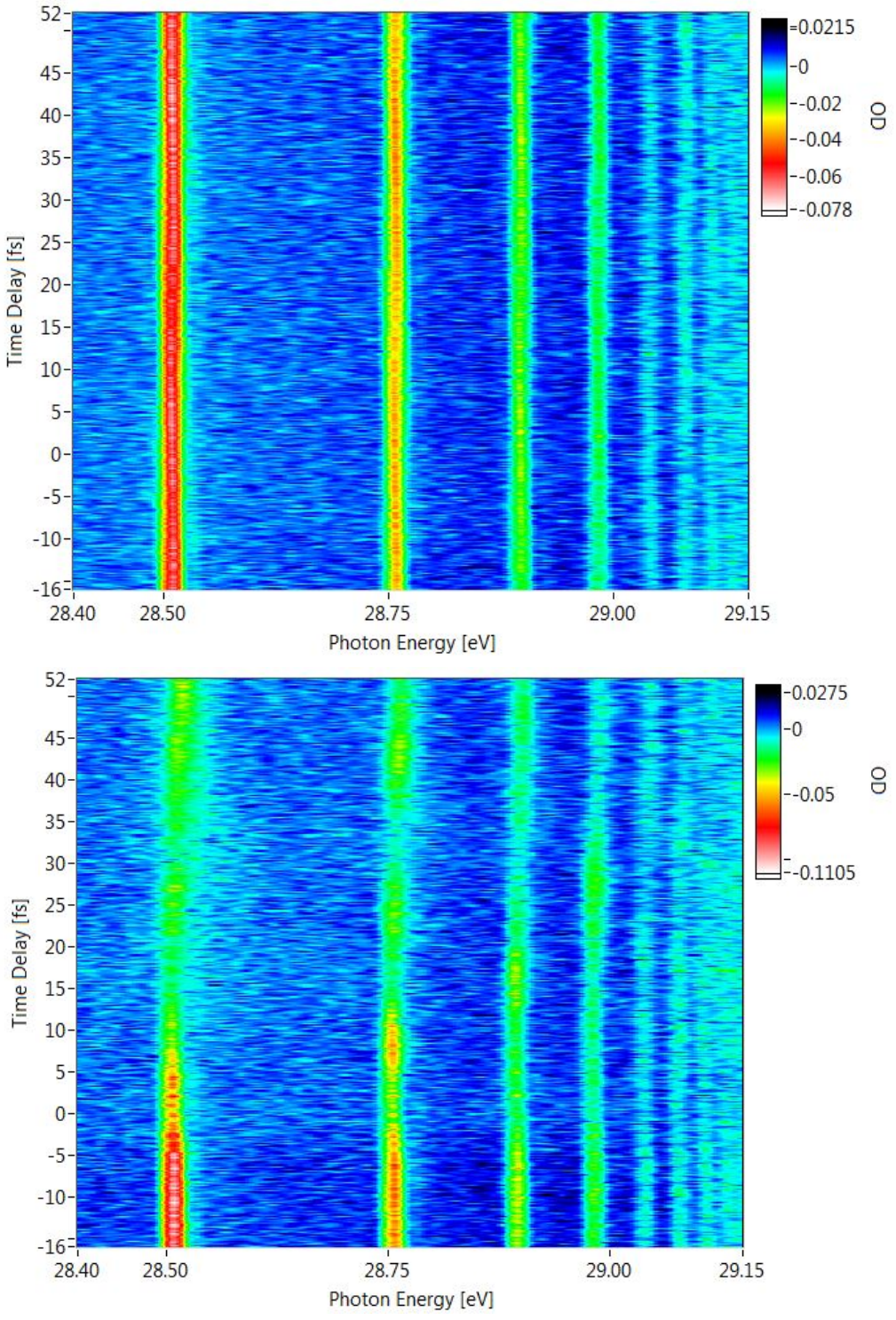

Figure 5.14: XUV absorption spectra of the higher-lying window resonances starting from the 6p state at intensities $1.5 \cdot 10^{11} W/cm^2$ and $5 \cdot 10^{12} W/cm^2$.

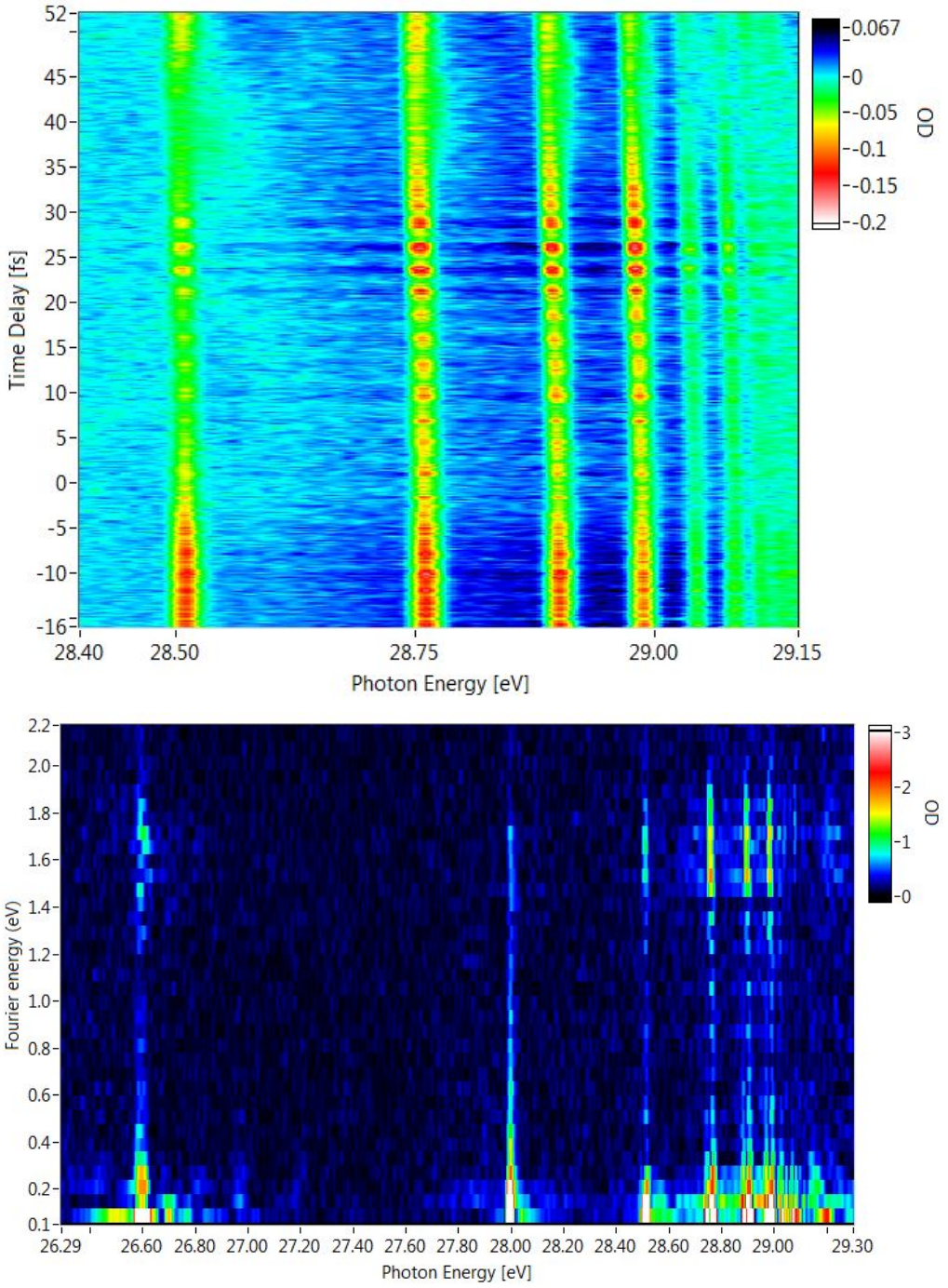

Figure 5.15: Absorption spectrum at intensity $5.4 \cdot 10^{12} W/cm^2$, with the corresponding Fourier transformed spectrum.

states. This line shape is kept for most of the positive time delays, but it is lost and suppressed at some time delays due to oscillations.

The second window resonance in the series, at the energy of 28 eV, is shown in figure 5.13. This line exhibits much less broadening than the already seen 4p line. The line starts splitting at intensity $3.9 \cdot 10^{12} W/cm^2$ which is higher intensity than in the case of the first line. The line shifts to higher energies for a more positive time delay. This line also has oscillations with Fourier energies below 0.5 eV and 1.5 and 1.7 eV, where I would use the same arguments for these oscillations as for the above described 4p resonance. The only problem is that there are no known dark states that this resonance could possibly couple to in the energy region of one NIR photon energy away from the line. This oscillation with Fourier energy of 1.7 eV hints that in some way the first two window resonances are coupled.

Finally, the higher-lying resonances are shown in figure 5.14. Almost no changes or oscillations at weaker intensity are visible for all the higher-lying states starting from the 6p state. However as the intensity increases the lines start shifting, broadening and even splitting at some positive time delays. The oscillations start being more pronounced, where at highest intensity they start oscillating at Fourier energy of 1.5 - 1.7 eV, which is shown in figure 5.15.

As I said in the introduction of the chapter, there exists only one scientific paper [24] that has published experimental results on argon window resonances with ATAS, and I will introduce it here. The research of this paper represents a first measurement of time-resolved autoionization of atoms with ATAS, which make it a pioneering experiment.

The differences between our work and theirs, apart from the experimental setup, are in that they have an isolated attosecond pulse, they have different NIR pulse parameters, with 1.65 eV central photon energy and 6 to 8 fs long pulses. Their spectrometer resolution was estimated to be 50 meV by using the 5p peak (Γ=28.2 meV) as a reference.

In fig 5.16 c) the transmitted XUV signal at the energy of the unpreturbed peaks 4p and 5p is plotted as a function of the delay. When the XUV and NIR overlap temporally the transmitted signal is minimized. The asymmetric weakening of the signal is fit very well using a cross-correlation of an exponential function with the state lifetimes and a Gaussian beam. As you have noticed from the lineout in fig. 5.8 our transmitted signal shows a different behavior where there is a dip at a small negative time delay, and the transmitted signal is not recovering much at large time delays.

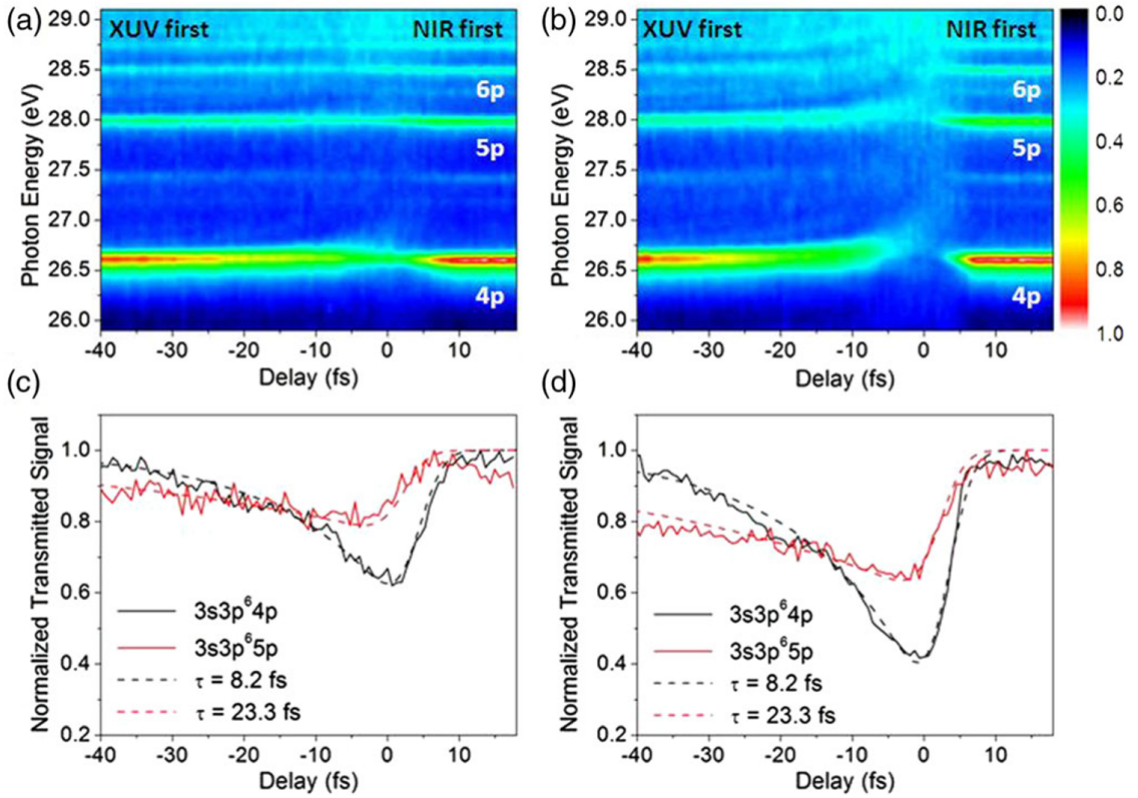

Figure 5.16: Transmitted XUV spectra of argon with a peak NIR intensity of a) $5 \cdot 10^{11} W/cm^2$ and b)$10^{12} W/cm^2$. Negative delays mean that the XUV pulse is arriving on the target first. c) and d) Transmitted signal(solid) near the $3s3p^6 4p$ and $3s3p^6 5p$ states for the intensites above, respectively, and calculated exponential decay convolved with 4.5 fs Gaussian for best fit(dashed). Taken from [24]

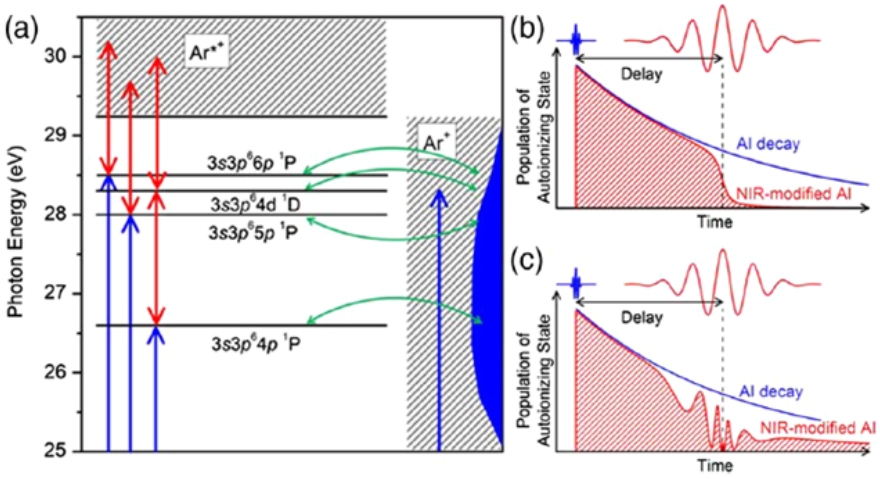

Figure 5.17: a) Level scheme of argon autoionizing states. The blue arrows indicate the attosecond XUV excitation of the ground state to the $3s3p^6np$ states and to the $Ar^+(3s^23p^5\varepsilon l)$ continuum. The red arrows indicate the driving laser coupling between the autoionizing states and $Ar^{*+}(3s3p^6\varepsilon l)$ continuum or to $3s3p^6nl$ autoionizing states. The configuration interaction (green arrows) couples all autoionizing states to the Ar^+ continuum. b) Autoionization decay modified by laser-induced coupling to the Ar^{*+} continuum. Ionization by the NIR field truncates the decay, shortening the lifetime of the state. c) Same decay modified by NIR-induced coupling to $3s3p^6nl$ states. Rabi oscillation between the two states results in ac Stark-like splitting. Taken from [24]

Conclusion

A one year's work on the Master's project and thesis has been presented in the past sixty pages. The main focus of my thesis was to probe the autoionizing states of argon, which came out to be successful with some peculiarities that are ubiquitous and natural to the measurement process. Some measurement parameters should have been changed to improve the measurement. As you have read, different sorts of complications with the measurement apparatus can arise, which is why one should take a great deal of attention and focus when it comes the performing such a measurement. Since there wasn't enough time to more thoroughly evaluate this measurement which was only done a little more than a month ago, I presented a mostly hypothetical description of the effects observed, where there are many questionable statements and occurrences in the data. The data seems to partly agree with the data from the published measurements on these states, although there are a lot more effects in this measurement. There is also a possibility of performing a few-level simulation in order to compare it to the experimental data, which didn't turn out to reproduce a good match for the published measurement in argon. Hopefully, many more new measurements are going to happen, what can help to clarify the complex strong-field driven electron dynamics of many-electron atoms. Within this work, an in situ calibration of the driving laser intensity has been performed, which followed the earlier developed method of calibration, with slight modifications. It is shown that the method is not the most accurate, where it is difficult to estimate the exact uncertainty of some pulse parameters like photon energy and pulse duration at target position. We should thus take advantage of the possibility of streaking in the lab in order to better characterize our laser pulses, which turns out to be key thing and a foundation for understanding transient phenomena happening on the microscale of the building blocks of matter.

Acknowledgements

First of all, I would like to thank the whole group for treating me nicely, and making me feel welcome and feel like part of the group.
I would like to thank Paul Birk for always being there for me, no matter what I asked him, he had a hard time refusing to help. I'm very thankful to you, for making me learn and understand things better, especially in the lab, where I felt the need to know more and more. I hope you continue to help others the way you helped me.
I'd like to thank you Christian Ott, for your support and incentive throughout the whole year I've spent here. It would have been much more challenging for me to make progress if it hadn't been for you to advise me and teach me in a wonderful way.
I'm not leaving out Veit Stooss, Thomas Ding, Max Hartmann,Alex Blaetermann and Gergana Borisova for a lot of help, good advice and company all along. Thank you to all the others who have been there and helped me.
I thank my friend Marko Petric for being by my side during my studies, a good honest fellow student.

I want to thank Thomas Pfeifer for letting me be part of the group, where I learned that it takes hard work and persistence to achieve goals. I learned so much about physics and the life of a physicist. This made me realize what physics represents to me, and the potential that exists. Thank you Robert Moshammer for accepting to be my examiner.
I want to thank my family for being there for me whenever I needed them, for the support and love they give me.

Bibliography

[1] Z. Chang *Fundamentals of attosecond optics* 2011 by Taylor and Francis Group, LLC

[2] A. Wirth et al. , *"Synthesized light transients"* Science 14 Oct 2011: Vol. 334, Issue 6053, pp. 195-200

[3] Adam Borzsonyi, *What We Can Learn about Ultrashort Pulses by Linear Optical Methods* Appl. Sci. 2013, 3, 515-544

[4] Masayuki Kakehata et al., *Carrier-envelope-phase stabilized chirped-pulse amplification system scalable to higher pulse energies* 2004 OSA / Vol. 12, No. 10 / OPTICS EXPRESS 2070

[5] Keldysh L V, *1964 Zh. Eksp. Teor. Fiz. 47 1945* Keldysh L V, 1965 Sov. Phys. JETP 20 1307 (Engl. transl.)

[6] A. Wirth, *Attosecond Transient Absorption Spectroscopy.* PhD thesis, LMU Munchen (2011).

[7] F. Krausz, M. Ivanov, *Attosecond physics.* Rev. Mod. Phys., vol. 81, no. 1, pp. 163234, 2009

[8] Baltuska et al. , *Attosecond control of electronic processes by intense light fields.* NATURE —VOL 421 — 6 FEBRUARY 2003.

[9] U. Fano *Effects of Configuration Interaction on Intensities and Phase Shifts.* Phys. Rev. **124**, 6 (1961).

[10] P. Lambropoulos and P. Zoller. *Autoionizing states in strong laser fields.*. Phys. Rev. A **24**, 379–397 (1981).

[11] M. Wu et al., *Theory of strong-field attosecond transient absorption.* J. Phys. B: At. Mol. Opt. Phys. 49 (2016) 062003

[12] C. Ott, A. Kaldun, P. Raith, K. Meyer, M. Laux, J. Evers, C. H. Keitel, C. H. Greene, and T. Pfeifer. *Lorentz Meets Fano in Spectral Line Shapes: A Universal Phase and Its Laser Control.* Science **340**, 716–720 (2013)

[13] R.H. French et. al, *Solar Energy Materials and Solar Cells 95 (2011) 20772086*

[14] Argenti et al. *Dressing effects in the attosecond transient absorption spectra of doubly excited states in helium.* Phys. Rev. A 91 061403

[15] M. Hartmann *Characterization of Few-Cycle Laser Pulses.* Master's thesis, Ruperto-Carola-University of Heidelberg, Germany (2016).

[16] C. Ott, *Attosecond multidimensional interferometry of single and two correlated electrons in atoms.* PhD thesis, Ruperto-Carola-University of Heidelberg, Germany (2012).

[17] G. Borisova *Theoretical and Experimental Studies of XUV Multielectron (Auto-)Ionization Dynamics in Helium and Molecular Hydrogen.* Master's thesis, Ruperto-Carola-University of Heidelberg, Germany (2017).

[18] https://www.tedpella.com/tape html/tape.htm

[19] http://henke.lbl.gov/optical constants/filter2.html

[20] A. Blaettermann et al. *In situ characterization of few-cycle laser pulses in transient absorption spectroscopy.* Vol. 40, No. 15 / August 1 2015 / Optics Letters

[21] Sorensen et al. *Argon 3s autoionization resonances.* Phys. Rev. A volume 50, 2 (1994)

[22] Berrah et al. J. Phys. B: At. Mol. Opt. Phys. 29 5351 (1996)

[23] Zhu-Lin-Fan et al 2003 Chinese Phys. Lett. 20 1718

[24] He Wang *Attosecond Time-Resolved Autoionization of Argon* PRL 105, 143002 (2010)

Erklärung:

Ich versichere, dass ich diese Arbeit selbstständig verfasst habe und keine anderen als die angegebenen Quellen und Hilfsmittel benutzt habe.

Heidelberg, den 22.December 2017 .....